Science Advances MAAAS

1 2	The reduce	ed net carbon uptake over northern hemisphere land causes the close-to-normal CO2 growth rate in							
3	2021 La Niña								
4 5	Iuniie I iu	1.2*, David Baker ³ , Sourish Basu ^{4,5} , Kevin Bowman ¹ , Brendan Byrne ¹ , Frederic Chevallier ⁶ , Wei He ⁷ , Fei							
_	•								
6	Jiang ⁷ , Matthew S. Johnson ⁸ , Terence L. Kubar ^{9,1} , Xing Li ¹⁰ , Zhiqiang Liu ¹¹ , Scot M. Miller ¹² , Sajeev Philip ¹³ ,								
7		Jingfeng Xiao ¹⁴ , Jeongmin Yun ¹ , Ning Zeng ^{15,16}							
8									
9	1.	Jet Propulsion Laboratory, California Institute of Technology, Pasadena, CA, USA.							
10	2.	Division of Geological and Planetary Sciences, California Institute of Technology, Pasadena, CA, USA							
11	3.	Cooperative Institute for Research in the Atmosphere, Colorado State University, Fort Collins, CO,							
12		USA.							
13	4.	NASA Goddard Space Flight Center, Global Modeling and Assimilation Office, Greenbelt, MD, USA.							
14	5.	Earth System Science Interdisciplinary Center, College Park, MD, USA.							
15	6.	Laboratoire des Sciences du Climat et de L'Environnement, LSCE/IPSL, CEA-CNRS-UVSQ,							
16		Université Paris-Saclay, 91191 Gif-sur-Yvette, France.							
17	7.	Nanjing University, Nanjing, China.							
18	8.	Earth Science Division, NASA Ames Research Center, Moffett Field, CA, USA.							
19	9.	Joint Institute for Regional Earth System Science & Engineering, University of California, Los Angeles							
20	10.	Research Institute of Agriculture and Life Sciences, Seoul National University, Seoul, Republic of							
21		Korea.							
22	11.	Laboratory of Numerical Modeling for Atmospheric Sciences & Geophysical Fluid Dynamics, Institute							
23	12	of Atmospheric Physics, Chinese Academy of Sciences, Beijing, China.							
24 25	12.	Department of Environmental Health and Engineering, Johns Hopkins University, Baltimore, MD 21218, United States of America.							
25 26	13	Centre for Atmospheric Sciences, Indian Institute of Technology Delhi, New Delhi, India.							
20 27		Earth Systems Research Center, Institute for the Study of Earth, Oceans, and Space, University of New							
28	17.	Hampshire, Durham, NH 03824, USA.							
29	15	Department of Atmospheric and Oceanic Science, University of Maryland, USA.							
30		Earth System Science Interdisciplinary Center, College Park, MD, USA.							
31	10.	Zana system settence intermisesprimary center, configer and, 112, configer							
32	*Correspond	ding author. Email: junjie.liu@jpl.nasa.gov							
33		rights reserved.							
34	_								

Abstract

La Niña climate anomalies have historically been associated with significant reductions in the atmospheric CO₂ growth rate. However, the 2021 La Niña exhibited a unique near-neutral impact on the CO₂ growth rate. In this study, we investigate the underlying mechanisms by employing an ensemble of net CO₂ fluxes constrained by CO₂ observations from the Orbiting Carbon Observatory-2 in conjunction with estimates of gross primary production, and fire carbon emissions. Our analysis reveals that the close-to-normal atmospheric CO₂ growth rate in 2021 was the result of the compensation between increased net carbon uptake over the tropics and reduced net carbon uptake over the northern hemisphere mid-latitudes. Specifically, we identify that the extreme drought and warm anomalies in Europe and Asia reduced the net carbon uptake and offset 72% of the increased net carbon uptake over the tropics in 2021. This study contributes to our broader understanding of how regional processes can shape the trajectory of atmospheric CO₂ concentration under climate change.

One-sentence summary:

The reduced carbon uptake in the northern hemisphere led to the near-normal CO₂ growth rate in 2021.

Science Advances Page 2 of 47

Introduction

Anthropogenic emissions from fossil fuel burning, cement production, and land use practices are primary drivers for the atmospheric CO₂ increase. However, not all anthropogenic emissions remain in the atmosphere. Remarkably, land and ocean have absorbed a stable proportion of the anthropogenic emissions so far, maintaining a roughly 44% airborne fraction (AF) (1), defined as the ratio between the annual increase in atmospheric CO₂ and the anthropogenic emissions (Figure 1). The AF has large year-to-year-variations, ranging from as low as approximately 20% to as high as 78% (Figure 1). This variation is mainly driven by the response of tropical land carbon fluxes to climate anomalies caused by the El Niño Southern Oscillation (ENSO) cycle (2–4). During El Niños, tropical continents are generally warmer and drier, leading to a decrease in carbon uptake from the atmosphere. This, in turn, results in a higher atmospheric CO₂ growth rate and an average of 16% more carbon remaining in the atmosphere (i.e., 60% AF) than the average. Conversely, La Niña events have the opposite effect, causing an average of 9% lower AF compared to the overall average (Figure 1). Therefore, the extent to which land absorbs carbon from the atmosphere and sustains a larger carbon sink in future La Niña events has significant implications for climate change and the effectiveness of carbon-climate policies aimed at achieving Paris climate goals.

In 2021, despite being in the middle of the longest La Niña event of this century (28 months) (Figure S1), the atmospheric CO₂ growth rate (Table S2) was surprisingly close to historical average, instead of being lower as expected from the historical record (Figure 1). Since the inception of the modern CO₂ records in 1959, the atmospheric CO₂ growth rate has, on average, been about 0.3 parts per million (ppm) lower than the climatological mean during La Niña events after removing the secular trend (Figure 1). For example, in 2011, the second longest La Niña event of this century, the atmospheric CO₂ growth rate anomaly was notably negative at -0.5 ppm and the AF at 32%, owing to the anomalous large carbon uptake over southern hemisphere semi-arid vegetation (5). Intriguingly, the atmospheric CO₂ growth rate anomaly in 2021 was a mere 0.01 ppm, and the AF was 46%, even higher than the average AF. This unique occurrence contrasts sharply with the historical pattern where positive CO₂ growth rate anomalies during La Niña events were extremely rare, with notably anomalies of 0.05 ppm in 1975 and 0.19 ppm in 1985.

Understanding the underlying factors contributing to the near-neutral impact of 2021 La Niña can provide valuable insights into the potential response of the carbon cycle to similar La Niña events and anticipated trajectories of atmospheric CO₂ concentration in the future. El Niño events, known for their significant influence on both precipitation and tropical carbon cycle, have garnered substantial interest within the scientific community (6–11). Conversely, research on La Niña events are relatively scarce (5). Unlike in 1975 and 1985, in 2021, there were unprecedented CO₂ observations from satellites. Previous studies have shown that the satellite observations from the Orbiting Carbon Observatory-2 (OCO-2) effectively monitored the response of regional carbon fluxes to climate interannual variations (9, 11–13).

In this study, we employ an ensemble of CO₂ fluxes estimated from top-down atmospheric inversions assimilating OCO-2 land observations (Table S1-S2). We also utilize two satellite-constrained gross primary production (GPP) products and a fire CO₂ emission product from a top-down CO atmospheric inversion (Methods and Table S2) to explore processes that have contributed to the close-to-average atmospheric CO₂ growth rate in 2021 La Niña condition. Specifically, our aim is to assess the land carbon cycle responses at various scales, ranging from hemispheric to

Science Advances Page 3 of 47

continental scales and then down to regions impacted by extreme climate anomalies. Additionally, we seek to quantify the role played by different vegetation types to examine whether semi-arid regions play an outsized role, as observed in the 2011 La Niña. The ensemble net CO₂ fluxes over 2015-2021 were generated with a subset of models that contributed to the v10 Orbiting Carbon Observatory (OCO-2) modeling inter-comparison project (MIP) by Byrne et al. (14) and one additional model, GCASv2, which has been documented in (15, 16). The ensemble top-down inversions capture the sensitivity of flux estimates to transport models, inversion methods, and inversion setups (Methods) (Table S1). The annual net carbon fluxes, calculated as the sum of fossil fuel emissions and natural carbon fluxes over land and ocean, align closely with the annual CO₂ growth rate reported by NOAA (Figure S2) (Methods).

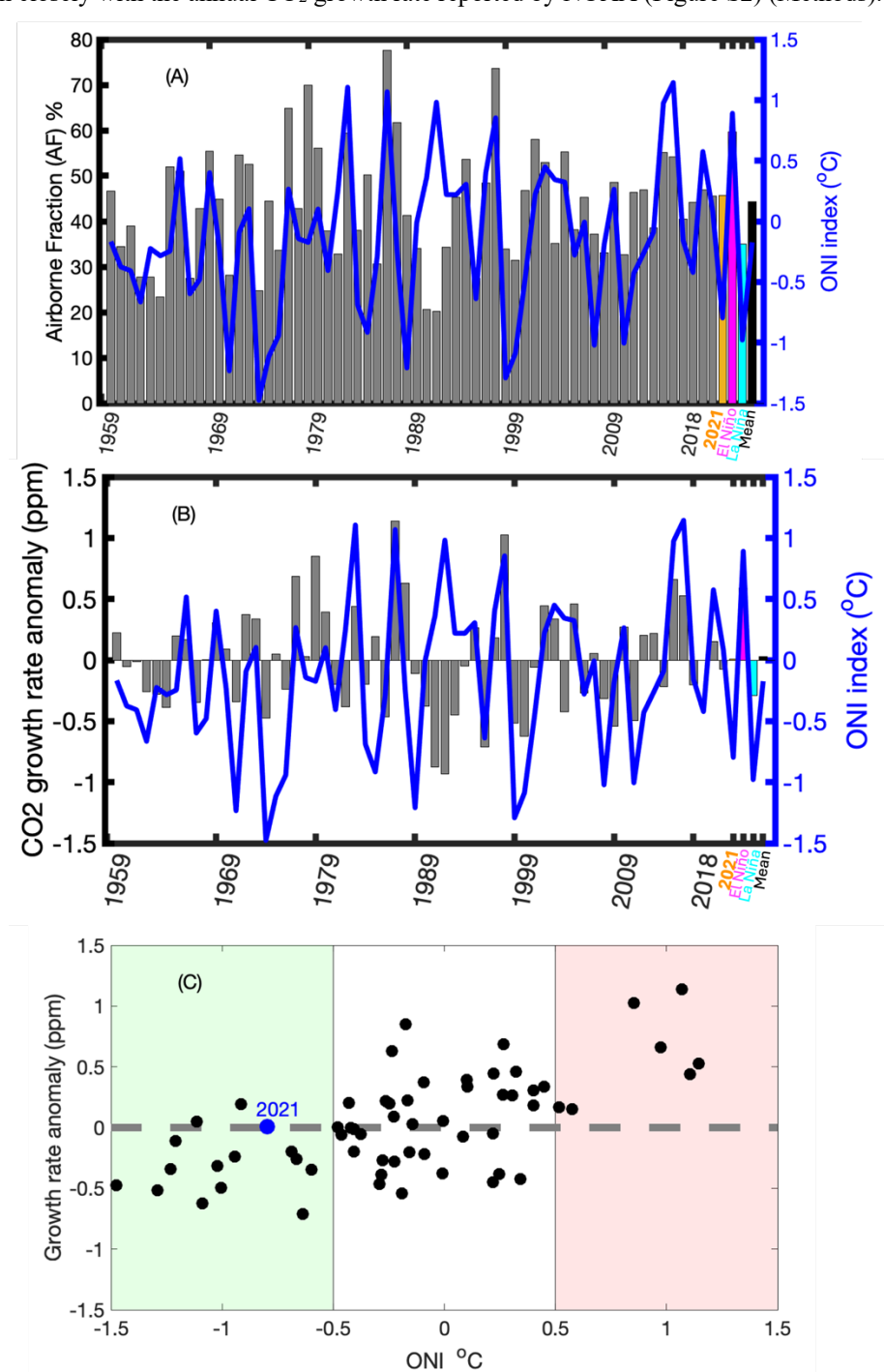


Figure 1. The atmospheric CO₂ growth rate and airborne fraction (AF) are generally lower during La Niña, while the growth rate in 2021 is close to average despite being in the middle of the longest La Niña in this century.

(A) Airborne fraction (bars) and annual mean Oceanic Nino Index (ONI) (Oct-Sep) (unit: °C) between 1959-2021

Science Advances Page 4 of 47

(line). Grey bars: 1959-2020; orange: 2021; cyan: average AF during La Niña events; magenta: average AF during El Niño events; black: average over 1959-2021; (B) CO₂ growth rate anomaly (black) (unit: ppm) and annual mean Oceanic Nino Index (ONI) (Oct-Sep) (unit: °C) between 1959-2021. (C) annual ONI index vs. CO₂ growth rate anomaly between 1959-2021 without 1991 and 1992, when Pinatubo volcano eruption had a dominant impact (17). ONI is defined as sea surface temperature (SST) anomalies over Niño 3.4 region (5°N-5°S, 170°W-120°W). El Niño years are those with annual mean ONI greater than 0.5°C, and La Niña years are those with annual mean ONI lower than -0.5°C. Note that the annual mean ONI is the mean over Oct-Sep to account for possible lagged response of land climate anomalies to SST anomalies (18), while the annual CO₂ growth rate for a given year is the CO₂ difference between the end of December and the start of January of that year based on global marine surface data (https://gml.noaa.gov/ccgg/trends/gl gr.html).

Results

Responses of hemispheric land carbon fluxes to 2021 La Niña

We calculated annual carbon flux anomalies relative to the mean over 2015 – 2021 for each year. Over these seven years, the land net biosphere exchange (NBE) (i.e., including all land-atmosphere CO₂ fluxes except fossil fuel emissions) dominated the year-to-year variations of total natural (land and ocean) carbon fluxes (Figure 2A), consistent with the long-established understanding that the NBE has stronger interannual variations than the ocean net carbon fluxes (19–22). In 2021, the NBE anomaly was -0.22±0.15 GtC, with negative numbers indicating more net carbon uptake from the atmosphere. Despite 2021 being the strongest La Niña among these seven years (Figure 1) (23, 24), the magnitude of net land carbon uptake from the atmosphere was smaller than that in 2017 and 2018 (Figure 2), which were weak La Niña during part of the year and had -0.74±0.14 GtC and -0.59±0.15 GtC NBE anomalies, respectively.

Breaking down the land into tropics and extra-tropics, we find that the tropical land absorbed 0.79 ± 0.23 GtC more carbon from the atmosphere in 2021, the largest carbon sink during these seven years, consistent with the notion that a larger carbon sink exists over the tropical land during La Niña years (3). Here the tropical land is defined as the land area within 22°S and 22°N. This increased net carbon uptake in 2021 had a similar magnitude as the anomalous carbon release from the tropical continents during the 2015-2016 El Niño, indicating the strong impact of climate interannual variations due to the ENSO cycle on tropical land carbon fluxes.

However, the extra-tropical land absorbed 0.57±0.30 GtC less carbon from the atmosphere in 2021 (Figure 2B), offsetting 72% of the increased carbon sink over the tropics. Consequently, land carbon sink only slightly increased in 2021 leading to a nominal CO₂ growth rate. The compensating carbon flux anomalies between the tropics and extra-tropics in 2021 were consistently estimated among all the inversions, and almost all the models indicate that the extra-tropics had the weakest carbon sink in 2021 (Figure S3). Note that the atmospheric CO₂ growth rate anomaly was calculated relative to the mean over 1959-2021 after removing the temporal trend, while the flux anomalies were calculated relative to the mean over 2015-2021, so the total flux anomaly in Figure 2 does not equal to the growth rate anomaly in Figure 1.

Previous studies suggest that the CO₂ flux distributions between the tropics and extra-tropics are affected by the errors in model-simulated CO₂ vertical profiles caused by vertical transport errors (25, 26). While the flux anomalies are found to be less sensitive to absolute errors in CO₂ vertical profiles, they could be influenced by the time-varying errors in CO₂ vertical gradient. To assess the robustness of the flux anomaly contrast between the tropics and extra-tropics, we quantified CO₂ vertical gradient errors across three regions – North America, Southeast Asia, and East Asia, where a stable amount of aircraft observations is available, and examined how the CO₂ vertical gradient errors vary by years

Science Advances Page 5 of 47

(Methods, Figures S4-S7). Remarkably, we found that the errors in CO_2 vertical gradient are relatively constant in each region over the period that we examined, although the absolute CO_2 vertical gradient errors differing by regions. For example, over southeast Asia, the CO_2 vertical gradient errors are 0.2 ± 0.3 ppm, 0.2 ± 0.3 ppm, and 0.4 ± 0.2 ppm in 2015, 2016, and 2017, respectively. This suggests that the impact of vertical transport errors on the flux distributions between the tropics and extra-tropics is consistent year-to-year, supporting the robustness of the flux anomaly contrast between the tropics and extra-tropics. The persistent nature of transport errors was also demonstrated in (27).

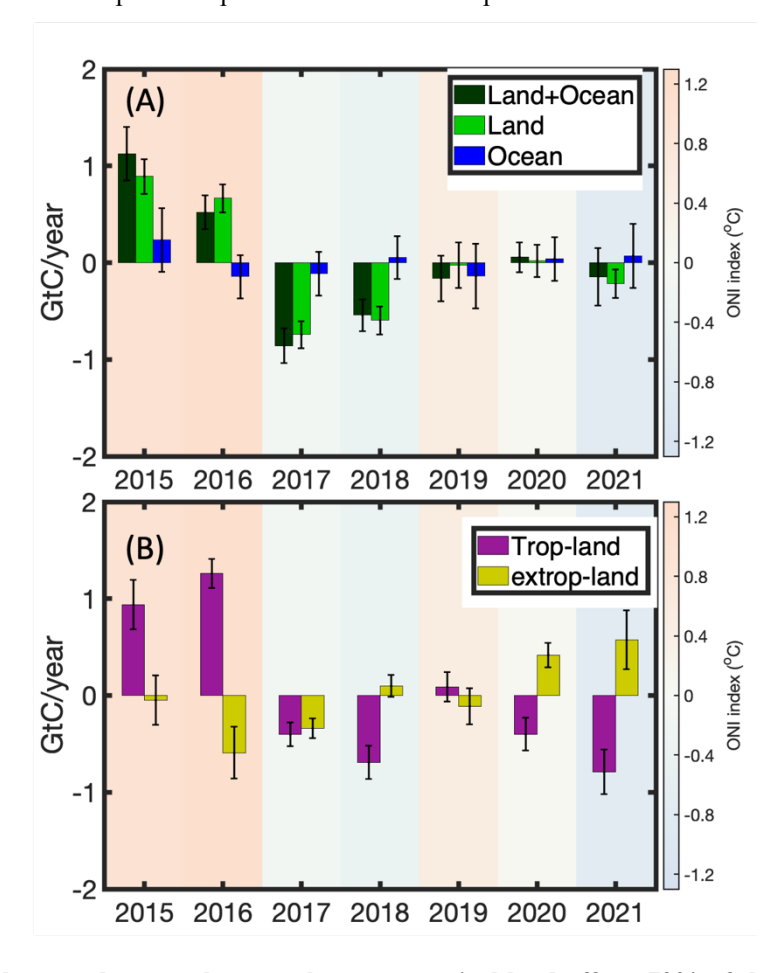


Figure 2 The reduced net carbon uptake over the extra-tropical land offsets 72% of the increased net carbon uptake over the tropical land, causing the close-to-average atmospheric CO₂ growth rate in 2021, despite being in the middle of the longest La Niña in this century. (A) annual combined land and ocean (dark green), land (light green), and ocean (blue) net carbon flux anomalies estimated by the ensemble top-down atmospheric inversion models (unit: GtC/year). (B) the annual net biosphere exchange (NBE) anomalies over tropical land (pink) and the extra-tropical land (yellow) (unit: GtC/year) from 2015-2021. Positive values indicate less carbon uptake from the atmosphere and vice versa. The sum of the NBE anomalies over the tropical land and the extra-tropical land in Panel (B) is equal to the total land NBE anomaly plotted in Panel (A). The background colors in these two panels are the annual ONI index, with red indicating positive sea surface temperature anomalies while blue to gray color indicating negative SST anomalies. Same as in Figure 1, the annual ONI is defined as mean SST anomalies between October and September in Niño 3.4 region. The uncertainty bars in the figures represent the standard deviations among the ensemble top-down atmospheric inversion models.

To further understand the causes for the reduced net carbon uptake over the extra-tropical land, we divided the extra-tropical land into three latitude bands: the Northern Hemisphere (NH) mid-latitudes (23°N-50°N), the NH high latitudes (50°N-90°N), and the Southern Hemisphere (SH) mid-to-high latitudes (23°S-60°S). We calculated net carbon flux and its component flux anomalies over forest, semi-arid region, and grassland/cropland (Figure S8). We find that the net carbon uptake over the NH mid latitudes reduced by 0.53±0.24 GtC in 2021, dominating the total net carbon uptake

Science Advances Page 6 of 47

reduction over the extra-tropics (0.57 ± 0.30 GtC) (Figure 3 and Figure S10). While over the SH mid-to-high latitudes, the net carbon uptake increased by 0.09 ± 0.04 GtC in the crop/grassland, and the net carbon uptake decreased by 0.15 ± 0.06 GtC over the NH high latitudes (Figure 3 and Figure S10), driven by the increased forest fire carbon emissions over Siberia forest (28). Since the magnitude of the net carbon flux anomalies over the SH mid-to-high latitudes and the NH high latitudes are much smaller, in the next two sections, we will focus on regional contributions and causes of net carbon flux anomalies over the tropics and the NH mid-latitudes.

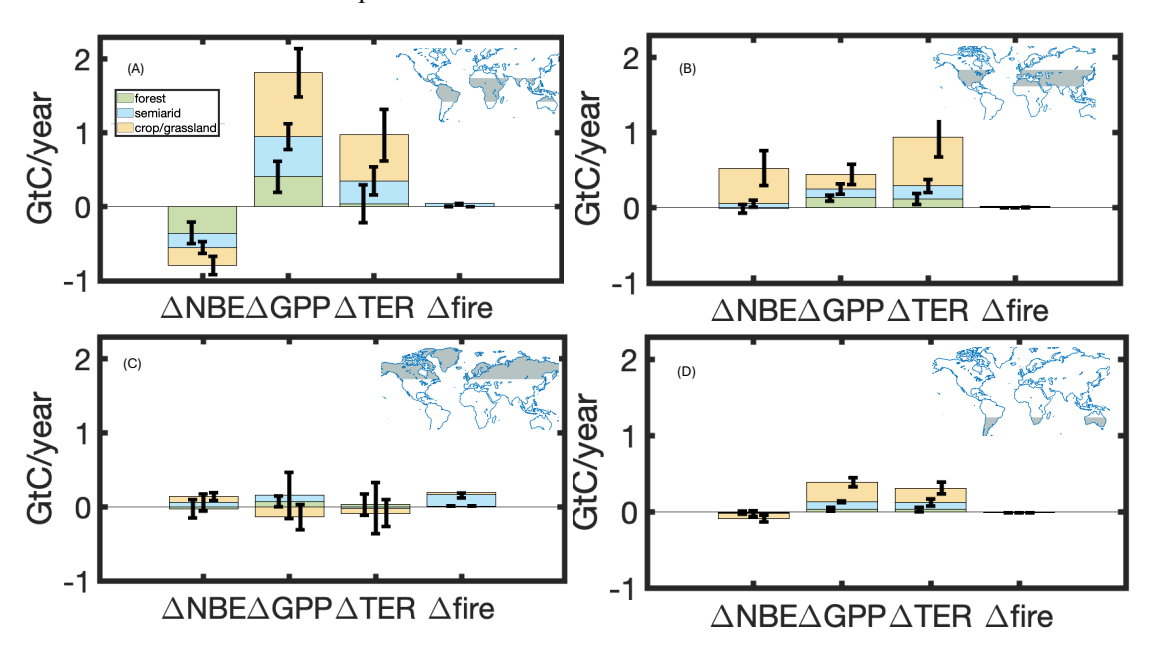


Figure 3 The reduction of net carbon uptake over the NH mid-latitudes has dominant contribution to the reduction of net carbon uptake over the extra-tropics. Forest over the tropics has a larger contribution to the tropical NBE anomalies than semi-arid region or grassland/cropland while almost all NBE anomalies occur over grassland/cropland over the extra-tropics. Annual net biosphere exchange (NBE), gross primary production (GPP), total ecosystem respiration (TER), and fire emission anomalies in 2021 over forest, semi-arid region, and crop land/grassland (the land cover type is based on MODIS IGBP 2020 land cover classification) in the tropics (A), the NH mid latitudes (B), the NH high latitudes (C), and the SH mid-to-high latitudes (D) (unit: GtC/year). The inserted plots on each panel indicate the regions each panel illustrates. A negative ΔNBE corresponds to an increased net carbon uptake from the atmosphere, while a positive ΔGPP indicates increased productivity. Conversely, positive ΔTER and $\Delta fire$ values suggest more carbon released to the atmosphere.

Regional contributions and causes of the increased net carbon uptake over the tropics in 2021

Over the tropics, Asia and south America had comparable increases in net carbon uptake, with -0.30 ± 0.13 GtC and -0.28 ± 0.15 GtC NBE anomalies, respectively (Figure 4). Tropical Africa exhibited a slightly lower increase, with -0.24 ± 0.13 GtC NBE anomaly. Of the -0.30 ± 0.13 GtC NBE anomalies occurred in tropical Asia, -0.07 ± 0.05 came from the tropical part of Australia, and the NBE anomaly over the rest of Australia was -0.07 ± 0.04 GtC. Thus, the NBE anomaly in Australia was -0.14 ± 0.06 GtC, weaker than the NBE anomalies over any of the tropical continents.

Nearly all NBE anomalies in tropical South America concentrated within the forested area, whereas semi-arid regions and grassland/cropland were the majority contributor to the net carbon flux anomalies over the tropical Africa and Asia (Figure 3). Only 10% of NBE anomalies over tropical Africa originated from forests, while approximately a quarter of the NBE anomalies in tropical Asia were observed in forested regions. In total, the forested regions contributed approximately 46% to the tropical NBE anomalies (Figure 3), while semi-arid and grassland/cropland regions contributed 25% and 30%, respectively.

Science Advances Page 7 of 47

 times of that over the forest region $(1.37 \pm 0.20 \text{ GtC vs.} 0.44 \pm 0.24 \text{ GtC})$ in the tropics (Figure 3). Most of the increase in GPP over the semi–arid region and grassland/cropland was released into the atmosphere through an increase in total ecosystem respiration (TER) (Figures 3 and 4) (Method), especially over grassland/cropland. This is likely due to the much shorter turnover time of carbon pools in these vegetation types (29).

However, the magnitude of GPP anomalies over the semi-arid region and grassland/cropland was approximately three

The increase in net carbon uptake across the three tropical regions was primarily driven by increased photosynthesis, corresponding to wetter conditions throughout the year in tropical South America and Asia (Figure S9-S12). However, tropical Africa experienced lower annual mean precipitation in 2021 compared to the mean over 2015-2021 (Figure S9-Figure S10). Despite this, the total water storage anomaly (TWS), indicating total soil water availability, was above average across most of tropical Africa throughout the year (Figure S11 and S13), potentially contributing to the observed increase in GPP over the region. Notably, Madani et al. (30) similarly noted that higher-than-average groundwater storage offsets the impact of precipitation deficit on GPP over African tropical forest. They found that GPP anomalies exhibit higher correlation with TWS anomalies than with precipitation anomalies over tropical Africa. This is likely due to deeper rooting zone water storage capacity and deeper rooting depth (31, 32)

The most substantial increase in GPP and net carbon uptake in the tropics were observed during the first half of the year and the last two months (Figure 5), coinciding with stronger La Niña and higher precipitation (Figure S1 and Figure S11-S12). Among all these regions, the precipitation increase in tropical South America was the most widespread and significant (Figure S9-S10). The anomalies in fire carbon emissions amounted to only 0.07 GtC across the entire tropics.

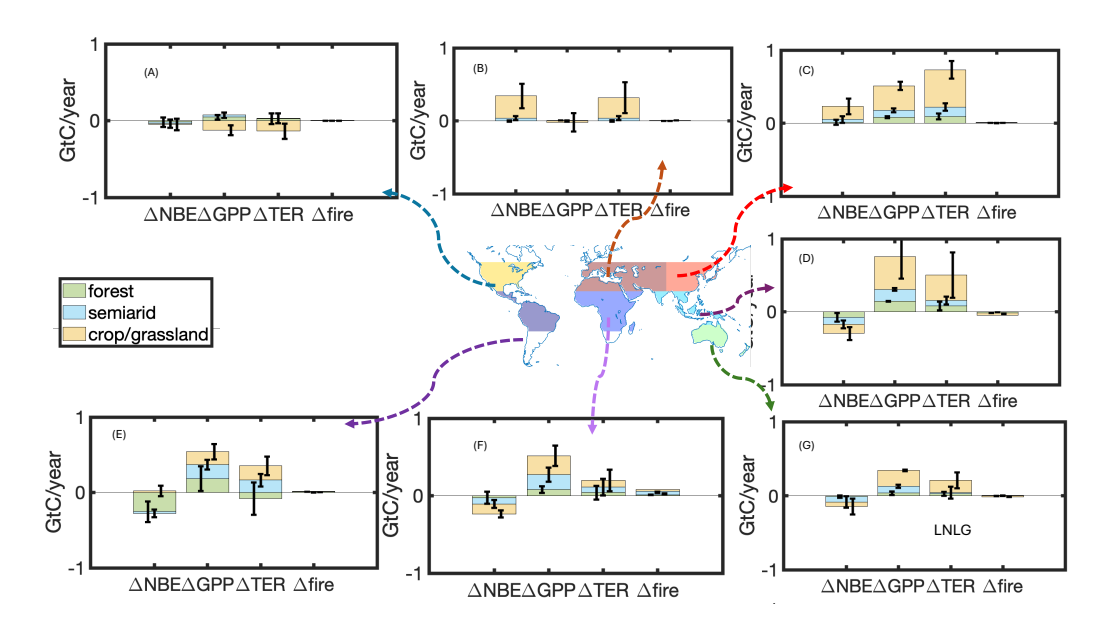


Figure 4 Tropical South America and Asia have comparable magnitudes of NBE anomalies. In tropical South America, forests predominantly contribute to these anomalies, whereas in tropical Africa and Asia, semi-arid regions and grassland/cropland play a dominant role. The overall reduction in net carbon uptake in extra tropical land regions, shown as positive NBE anomalies, is mainly driven by Europe and Asia. Annual anomalies of net biosphere exchange (NBE), gross primary production (GPP), total ecosystem respiration (TER), and

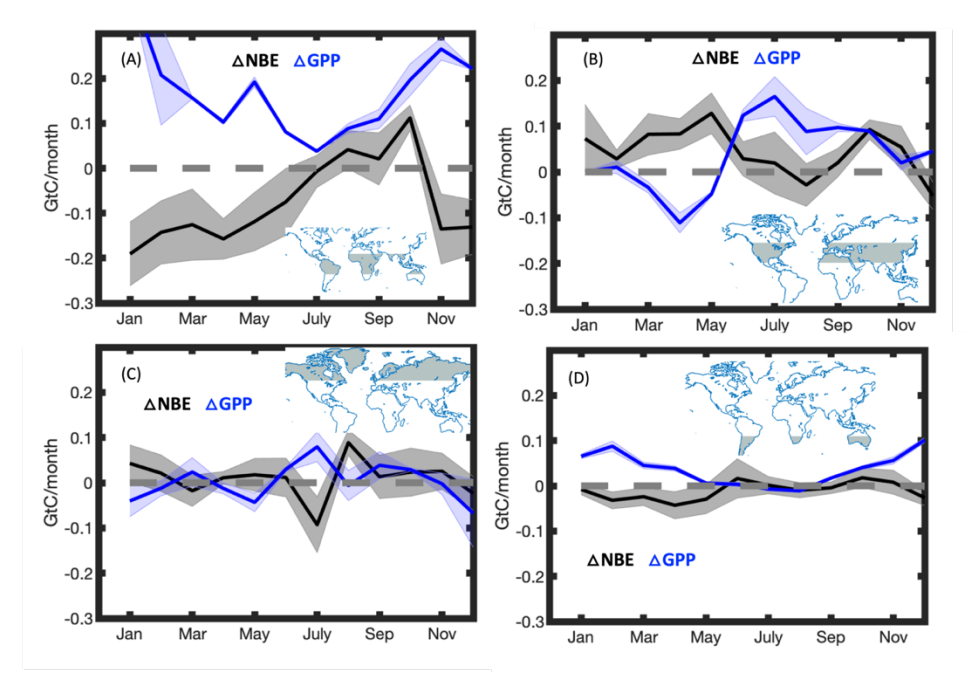


Figure 5 Independent monthly GPP anomaly and NBE anomaly show anti-correlation in all four latitude bands. (A), (B), (C), and (D): Monthly NBE (black) and GPP (blue) anomalies over the tropics, NH mid latitudes, NH high latitudes, and SH mid-to-high latitudes respectively (unit: GtC/month).

Regional contributions and causes of the deceased net carbon uptake over the NH mid-latitudes in 2021

Different from the tropics, over the NH mid-latitudes, the reduction in net carbon uptake (i.e., positive NBE anomalies) primarily occurred over grassland/cropland in Eurasia and East Asia (Figure 4). The total net carbon uptake over North America (NA) remained close to normal, primarily due to the compensating effect between the increased net carbon uptake in the east and reduced net carbon uptake in the west (Figure S9). In contrast to the tropics, the decrease in net carbon uptake over the NH mid-latitudes was driven by an increase in TER instead of a decrease in GPP (Figures 3 and 4), particularly over East Asia.

The reduction in net carbon uptake over Eurasia was predominantly observed in regions that experienced extreme climate anomalies in 2021, especially in central Asia (Figure 6). Averaged over April to June, the temperature anomalies reached up to 3°C above normal, while precipitation decreased by as much as 60-80% in central Asia (Figure 6). These extreme conditions resulted in reduced productivity and increase in ecosystem respiration (Figure 6). The GPP decreased by over 80% during April to June in a substantial area of central Asia (Figure 6). On an annual total, the net carbon uptake decreased by 0.39 ± 0.12 GtC between 35°E-85°E and 30°N-50°N, accounting for more than half of the total NBE anomalies over the NH mid latitudes. Approximately half of the NBE anomalies in this region can be attributed to a reduction in GPP (-0.20 ± 0.12 GtC), while the other half results from an increase in TER (0.19 ± 0.17 GtC). The contribution of fire emissions to the reduced net carbon uptake in this region is negligible.

In East Asia, annual GPP increased by 0.52 ± 0.07 , but the increase in TER was even larger, with a 0.77 ± 0.15 anomaly. Consequently, net carbon uptake decreased by 0.25 ± 0.12 GtC. The most significant reduction in net carbon uptake occurred during spring to early summer (Figure 7 and Figure S12), predominantly over central and northern China

Science Advances Page 9 of 47

(Figure 7). This corresponds to high temperature anomalies and reduced precipitation (Figure 7). During the summer, despite increased productivity in most of East Asia, the net carbon uptake decreased (Figure S12). This implies an increase in ecosystem respiration, possibly due to much warmer temperatures across the region and drier condition over southern China (Figure 7, Figure S9 and S13).

In addition to the ENSO cycle, various teleconnections, including Indian Ocean Dipole (IOD), North Atlantic Oscillation (NAO), and Arctic Oscillation (AO), have caused carbon flux anomalies over mid latitudes (34–36). However, in 2021, these teleconnections were observed to be within normal ranges (Figure S14), suggesting that the mid-latitude carbon flux anomalies in 2021 were not influenced by these teleconnections.

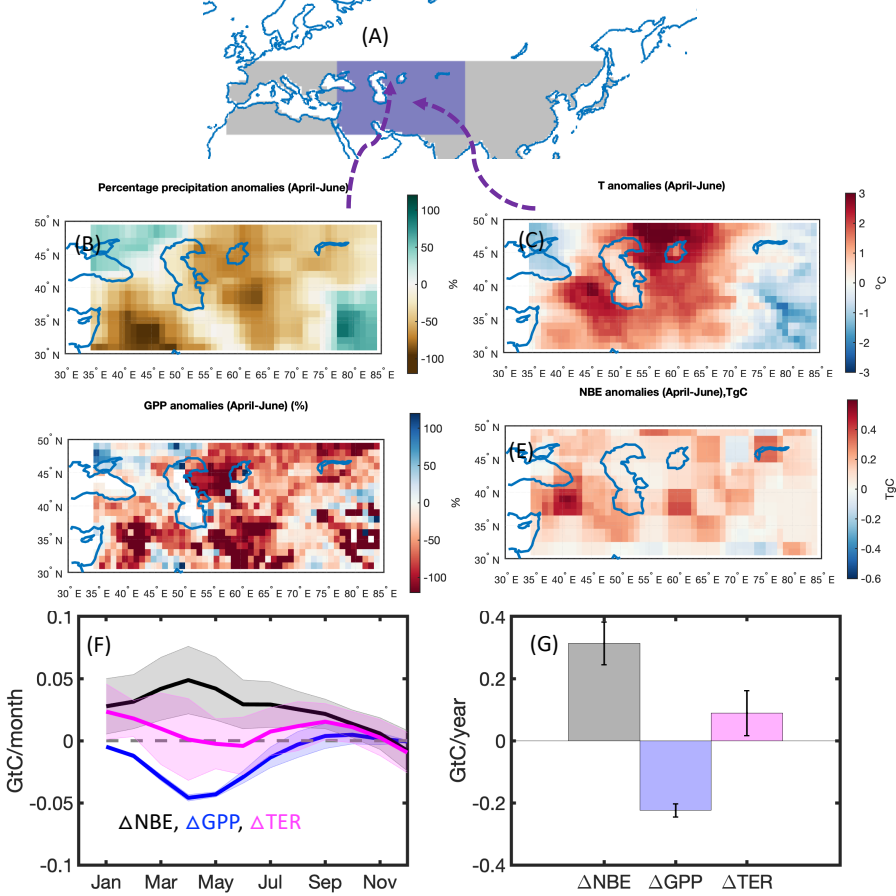


Figure 6 The extreme drought and warm climate anomalies cause the large reduction of gross primary production and increase of ecosystem respiration over central Asia, both of which contributes to the reduction of net carbon uptake over the region. (A) Regional mask for central Asia (purple) relative to Eurasia regional mask (grey). (B) Percentage precipitation anomalies between April-June, 2021 (unit: %) relative the mean over 2015-2021; (C) temperature anomalies between April-June; (D) percentage change of GPP anomalies between April-June (unit: %); (E) NBE anomalies during April-June (unit: tera grams of carbon (TgC)); (F) monthly anomalies of net biosphere exchange (NBE), gross primary production (GPP), and total ecosystem respiration (TER) over the region (unit: GtC/month); (G) annual anomalies of NBE, GPP, and TER (unit: GtC/year).

Science Advances Page 10 of 47

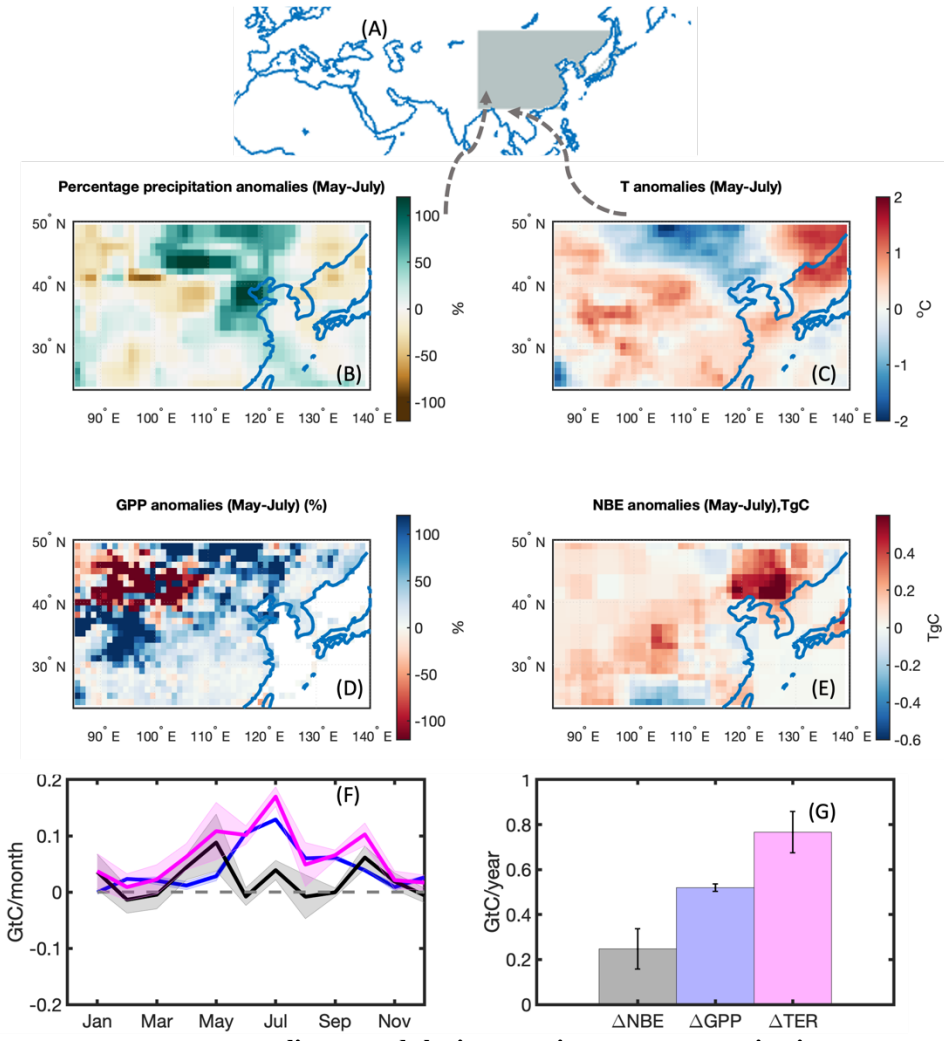


Figure 7 The warm temperature anomalies caused the increase in ecosystem respiration over east Asia, outpacing the GPP increase. (A) Regional mask for east Asia (grey). (B) Percentage precipitation anomalies between May-July, 2021 (unit: %) relative the mean over 2015-2021; (C) temperature anomalies between May-July; (D) percentage change of GPP anomalies between May-July (unit: %); (E) NBE anomalies during May-July (unit: tera grams of carbon (TgC)); (F) monthly anomalies of net biosphere exchange (NBE), gross primary production (GPP), and total ecosystem respiration (TER) over the region (unit: GtC/month); (G) annual anomalies of NBE, GPP, and TER (unit: GtC/year).

The impact of fossil fuel emission uncertainties on flux anomaly estimation over East Asia

Our results reveal a decrease in net carbon uptake in East Asia for the year 2021 despite increases in GPP. We posit that the higher-than-normal temperatures during spring and later in the year contribute to the elevated terrestrial biosphere respiration, ultimately leading to a reduction in net carbon uptake across the region.

However, it is crucial to acknowledge that this conclusion relies on the accuracy of fossil fuel emission anomalies used in the top-down inversions. We calculate NBE anomalies by subtracting fossil fuel emission anomalies from the total flux anomalies, assuming the accuracy of the former. This assumption is grounded in the observation that the relative uncertainties in fossil fuel emission inventories are smaller compared to natural carbon fluxes (19). Nonetheless, it is important to note that the relative uncertainties of fossil fuel emissions can be considerably much larger on regional scales (37, 38) and this uncertainty may be reflected in the NBE estimates.

Science Advances Page 11 of 47

Given East Asia's significant magnitude of fossil fuel emissions, totaling 3.5 GtC in 2021 based on ODIAC fossil fuel emission inventory (Figure S15), and the substantial uncertainties in emission trends, NBE estimates for this region may exhibit heightened vulnerability to uncertainties in fossil fuel emissions. To assess the potential impact of uncertainties in fossil fuel emissions on the calculation of NBE anomalies in East Asia, we compared the fossil fuel emissions used in our study with those from the GridFED fossil fuel emission inventory, as reported in GCP 2022 (19). In our investigation, all eight inversion models utilized the same fossil fuel emission data from ODIAC (refer to Methods and Table S1). The annual totals for both 2020 and 2021 were derived from near-real-time fossil fuel emission data from Carbon Monitor, and the spatial distribution was based on ODIAC.

Our findings indicate that the fossil fuel emission anomaly in 2021, relative to the mean between 2015 and 2021, is 0.17 GtC for both inventories over East Asia (Figure S15), consistent with each other, albeit with a mean difference of 0.1 GtC. Even at the monthly time scale, the fossil fuel emissions agree on the magnitude of anomalies, though they differ in their seasonality (Figure S16). Furthermore, the magnitude of monthly fossil fuel emission anomalies is much smaller than that of NBE anomalies (Figure S17). It is noteworthy that NBE anomalies are only responsive to fossil fuel emission anomalies, rather than being influenced by the absolute values of fossil fuel emissions. This is attributed to the removal of annual/monthly mean fluxes during the calculation of annual/monthly flux anomalies.

Assuming a 20% uncertainty in fossil fuel emission anomalies over East Asia, implying a range from 0.13 to 0.21 GtC for fossil emission anomalies, we propagated this uncertainty into the calculation of NBE anomalies. Consequently, the NBE anomalies over East Asia integrated over all vegetation types were determined to be 0.25 \pm 0.13 GtC, reaffirming their robustness.

Discussion

Comparisons to the response of terrestrial biosphere carbon cycle to the 2011 La Niña event

Our results reveal a substantial increase in the net carbon sink over tropical land in 2021, marking the most significant tropical carbon sink observed between 2015 and 2021. Conversely, the SH NBE anomaly is only -0.08±0.04GtC. Notably, the tropical forest contributes approximately 50% while the semi-arid region contributes 20-30% to the overall increased tropical and SH net carbon uptake anomalies. These results stand in stark contrast to what happens during 2011 La Niña, as highlighted by Poulter et al. (5). During 2011, NBE anomalies were primarily driven by increased net carbon uptake in semi-arid regions across the southern hemisphere, with Australia itself accounting for 60% of net carbon flux anomalies (18, 19). In contrast to the 2011 La Niña, only about 25% of the increased tropical net carbon uptake occurs over Australia in 2021 (Figures 3 and 4). This difference could be attributed to lower precipitation and higher temperature over Australia in 2021 compared to 2011. Relative to 2011, the precipitation over Australia was 32% lower and temperature was higher than 1.3°C (Figure S12).

Furthermore, in 2021, while the tropical GPP increase over semi-arid regions and grassland/cropland is significantly larger than that over forests, a substantial portion of the increased carbon accumulation resulting from photosynthesis is released back to the atmosphere through increased respiration, likely due to an increased carbon pool from increased GPP and favorable climate conditions.

Science Advances Page 12 of 47

The determination of whether forests or semi-arid regions serve as the primary drivers of net carbon flux interannual variability holds crucial implications for carbon-climate projections (16). This is because studies have shown that the response of carbon cycle to interannual climate variations are indicative of how carbon storage will respond to future climate change (39, 40). Thus, whether tropical forests or semi-arid regions have larger sensitivity to climate interannual variations would imply the vulnerability of their carbon storage to future climate change. The stark contrast of the response of tropical and SH land carbon cycle to the 2011 and 2021 La Niña events indicates that a long-term global CO₂ observation record that captures multiple ENSO cycles is essential to understand whether tropical forests or semi-arid regions exert primary influence on the net carbon flux interannual variability and the vulnerability of their carbon storage to future climate change.

Implications

The close-to-normal atmospheric CO₂ growth rate in 2021 was the result of the compensation between increased net carbon uptake over the tropics and reduced net carbon uptake over the NH mid-latitudes. Specifically, the extreme drought and warm anomalies over Europe and Asia reduced the net carbon uptake and offset 72% of the increased net carbon uptake over the tropics from the impact of the 2021 La Niña. By comparison, the atmospheric CO₂ growth rate was close to average in only two other La Niña events, 1975 and 1985 (Figure 1). During those two events, the precipitation anomaly over central Asia (30N-50N, 30E-85E) was -15.6% and -16.7% during April-July in 1975 and 1985 respectively, while the precipitation anomaly was -22.6% in 2021 (Figure S19 – S20). In 1985, the precipitation reduction was more than 50% over part of the central Asia, comparable to the precipitation anomaly in 2021 (Figure S18). We speculate that the close-to-normal CO₂ growth rate in these two years may also have been caused by the opposite net carbon flux anomalies between the tropics and extra-tropics.

The frequency of extreme La Niña events is projected to become more frequent in the future (41). At the same time, CMIP6 models predict that the annual and early summer precipitation over central Asia is positively correlated with the ONI, suggesting reductions of precipitation during extreme La Niña years over central Asia (Figure S21). Furthermore, positive vapor pressure deficit (VPD) anomalies especially during early summer are projected by CMIP6 models during La Niña years. With the simultaneously increase of global temperature and predicted drying trend in western US (IPCC AR6), our results imply that the regional compensation of flux anomalies between tropics and extratropics may become more frequent in future extreme La Niña events. The pivotal question of whether the CO₂ airborne fraction during La Niña events will remain lower than the average AF holds substantial implications for the trajectory of atmospheric CO₂ levels in the future. This underscores the critical importance to continue monitoring the natural carbon cycle at regional scales to inform and support effective carbon-climate policies.

Materials and Methods

1. Top-down atmospheric CO2 flux inversions with OCO-2 V10 MIP extension

In this study, the top-down fluxes were generated with eight inversion models that are a subset of the models participating in the v10 OCO-2 MIP described in Byrne et al. (14) plus GCAS v2 model that were documented in (15, 16). These inversions were extended to the end of 2021. They used a combination of four transport models, three types of inversion algorithms, and two sources of meteorology fields (Table S1). All the inversions used the same fossil fuel emissions and assimilated the same set of OCO-2 V10 retrievals (Table S2). Since the number of surface flask observations was drastically different in 2021 at the time of this study (May 2022) due to data latency, which may

Science Advances Page 13 of 47

impact the interannual variability analysis, we used the inversion results that assimilated OCO-2 V10 land retrievals only for the entire period (Jan 2015-Dec 2021) in the main text. The original fossil fuel emission has 1° x 1° resolution. The data between 2015-2019 was from the official ODIAC website (https://odiac.org/data-product.html), while the fossil fuel emissions for 2020 and 2021 is scaled ODIAC emission using the country totals published by Carbon Monitor (42). Both air-sea exchange and net biosphere exchange were optimized in these models, but the prior assumptions for these fluxes could be different (Table S1). Table S2 lists all the assimilated observations and their sources.

The spatial resolution of these eight models is different, but all the posterior fluxes from these inversions were regridded to 1° x 1° resolution before analysis. The global annual net carbon fluxes calculated as the sum of fossil fuel emissions and natural carbon fluxes over land and ocean are consistent with the NOAA annual CO₂ growth based on marine surface network (Figure S2). The NOAA annual CO₂ growth in parts per million (ppm) was converted to gigaton carbon per year (GtC/year) using the conversion factor 2.124 GtC/ppm (43). We assumed 0.2 GtC/year uncertainty for the observed annual CO₂ growth (19).

We calculated the mean across the ensembles as the best estimate and the standard deviation as the uncertainty. The uncertainties of top-down NBE estimation come from the uncertainties in atmospheric transport models, observations, assumed prior natural carbon fluxes, and fossil fuel emissions. Even though we only have eight ensemble members, these top-down inversion models used a variety of transport models, inversion methodologies, and prior natural carbon fluxes (Table S1). Thus, using ensemble standard deviations as NBE uncertainty enables us to capture the uncertainties in these aspects. However, since all these models used the same set of observations and fossil fuel emissions, the uncertainties in these aspects are not fully captured in the ensemble spread. As discussed in the section: "The impact of fossil fuel emission uncertainties on flux anomaly estimation over East Asia", the NBE anomalies analyzed in this study are more sensitive to changes of fossil fuel emissions, which are consistent among different fossil fuel mission products. The standard deviation among the ensemble inversions can still capture the uncertainties in observations, since the inversions assumed uncertainties (around 1-3 ppm) in these observations (14) even though all inversion models used the same set of observations. Note that the uncertainties estimated as the ensemble spread is different from uncertainties from individual models, which only include uncertainties in observations and prior fluxes and can significantly differ among each individual model (14).

We evaluated the posterior atmospheric CO₂ concentrations against observed CO₂ vertical profiles from ACT-America (44–47) campaign and CONTRAIL (48) included in (47) (Figures S4-S7), since previous research suggests that the partition of carbon fluxes over the tropics and extra-tropics is sensitive to errors in CO₂ vertical gradient. As we focus on the flux anomalies, the results are not sensitive to the absolute errors in CO₂ vertical gradient but are sensitive to time-varying errors. We chose measurements from these two aircraft measurements because of their consistent observation coverage. CONTRAIL has observations over all the months over 2015-2017 and ACT-America has observations between 2016 and 2019. Because of data latency, there is no CONTRAIL insitu profiles publicly available for 2019-2021 at the time of this study and ACT-America field campaigns ended in 2019. The flask observations collected by the National Institute for Space Research (INPE) over tropical South America might have higher measurement errors due to water vapor contamination, so we did not include those observations in the comparison.

Science Advances Page 14 of 47

Despite the errors in vertical CO₂ gradient in each region, the errors are relatively constant from year-to-year, which indicates that the contrast of flux anomalies between tropics and extra-tropics are robust.

30 31 32

33

34

35

36

37

29

2. GPP estimates

We used two gross primary production (GPP) products in this study: FluxSAT and GOSIF (20, 21) (Table S2). Both datasets were generated with machine learning approaches. FluxSAT was derived with neural networks that upscaled GPP from selected FLUXNET 2015 eddy covariance tower sites to a gridded global GPP with the input of Nadir Bidirectional Reflectance Distribution Function (BRDF)-Adjusted Reflectances (NBAR) product from the MODIS instruments on the NASA Terra and Aqua satellites (48). The FluxSAT provides global gridded daily estimates of GPP and uncertainties at 0.05-degree resolution.

38 39 40

41

42

43

44

GOSIF GPP was generated with the global, OCO-2 based SIF product (GOSIF) and linear relationship between SIF and GPP to map GPP globally at 0.05-degree resolution (49). GOSIF GPP product accounts for uncertainties of GPP estimates using eight SIF-GPP relationships with different forms. The GOSIF SIF product was generated with a machine learning approach that upscales OCO-2 SIF to a global product at 0.05-degree resolution with data from MODIS and meteorological reanalysis.

45 46

47

We regridded both products to 1° x 1° resolution and used the mean as the best estimate. We estimate uncertainties with a bootstrapping approach by randomly generating 1000 samples based on the difference between these two products.

48 49 50

53

3. Fire and total ecosystem respiration

- 51 The monthly fire CO₂ emissions were documented (50), and estimated with a top-down atmospheric inversion
- 52 assimilating CO observations from Measurements of Pollution in the Troposphere (MOPITT). (50) does not include
 - uncertainties, and we assumed a 20% uncertainty in the fire CO₂ emission anomalies. The total ecosystem respiration
- 54 (TER) was calculated as follows:
- 55 TER=NBE+GPP-FIRE
- The uncertainties for TER were calculated as:
- $R_{TER}^2 = R_{NBE}^2 + R_{GPP}^2 + R_{FIRE}^2$
- where R_{TER} , R_{NBE} , R_{GPP} , R_{FIRE} are uncertainties for TER, NBE, GPP, and fire respectively. Any fire-related land use
- 59 land cover change (LULCC) anomalies were included in fire emissions, which is the largest component in the
- 60 interannual variability of LULCC (51). Non-fire related LULCC anomalies were included in other carbon flux
- 61 components.

62 63

Since TER was calculated as the residual among NBE, GPP, and FIRE, we indirectly validated TER by validating NBE, GPP, and fire emissions. The GPP products have been validated against FLUXNET observations (49, 50). We validated NBE through comparison against aircraft observations. The fire emission data was used in Zheng et al. (28).

6566

64

References

67 68 69

Science Advances Page 15 of 47

- 1. Friedlingstein, P., Jones, M.W., O'Sullivan, M., Andrew, R.M., Bakker, D.C.E., Hauck, J., Le Quéré, C., Peters, G.P., Peters, W., Pongratz, J., Sitch, S., Canadell, J. G., Ciais, P., Jackson, R. B., Alin, S. R., Anthoni, P., Bates, N. R., Becker, M., Bellouin, N., Bopp, L., Chau, T. T. T., Chevallier, F., Chini, L. P., Cronin, M., Currie, K. I., Decharme, B., Djeutchouang, L. M., Dou, X., Evans, W., Feely, R. A., Feng, L., Gasser, T., Gilfillan, D., Gkritzalis, T., Grassi, G., Gregor, L., Gruber, N., Gürses, Ö., Harris, I., Houghton, R. A., Hurtt, G. C., Iida, Y., Ilvina, T., Luijkx, I. T., Jain, A., Jones, S. D., Kato, E., Kennedy, D., Klein Goldewijk, K., Knauer, J., Korsbakken, J. I., Körtzinger, A., Landschützer, P., Lauvset, S. K., Lefèvre, N., Lienert, S., Liu, J., Marland, G., McGuire, P. C., Melton, J. R., Munro, D. R., Nabel, J. E. M. S., Nakaoka, S.-I., Niwa, Y., Ono, T., Pierrot, D., Poulter, B., Rehder, G., Resplandy, L., Robertson, E., Rödenbeck, C., Rosan, T. M., Schwinger, J., Schwingshackl, C., Séférian, R., Sutton, A. J., Sweeney, C., Tanhua, T., Tans, P. P., Tian, H., Tilbrook, B., Tubiello, F., van der Werf, G. R., Vuichard, N., Wada, C., Wanninkhof, R., Watson, A. J., Willis, D., Wiltshire, A. J., Yuan, W., Yue, C., Yue, X., Zaehle, S., and Zeng, J. (2022) Global Carbon Budget 2021. Earth Syst. Sci. Data, 14, 1917–2005. https://doi.org/10.5194/essd-14-1917-2022
- 2. Zeng, N., Mariotti, A. and Wetzel, P. (2005) Terrestrial mechanisms of interannual CO2 variability. Global Biogeochem. Cycles, 19. https://doi.org/https://doi.org/10.1029/2004GB002273
- 3. Sellers, P.J., Schimel, D.S., Moore, B., Liu, J. and Eldering, A. (2018) Observing carbon cycle-climate feedbacks from space. Proc. Natl. Acad. Sci. U. S. A., 115. https://doi.org/10.1073/pnas.1716613115
- 4. Worden, J., Saatchi, S., Keller, M., Bloom, A., Fu, R., Worden, S., Liu, J., Parazoo, N., Fisher, J.B., Worden, H., Bowman, K., Reager, J.T., Fahy, K., Schimel, D., Fu, R., Worden, S., Yin, Y., Gentine, P., Konings, A.G., Quetin, G. R., Williams, M., Worden, H., Shi, M., Barkhordarian, A., (2021) Satellite Observations of the Tropical Terrestrial Carbon Balance and Interactions with the Water Cycle During the 21st Century. Rev. Geophys., n/a, e2020RG000711. https://doi.org/https://doi.org/10.1029/2020RG000711
- 5. Poulter, B., Frank, D., Ciais, P., Myneni, R.B., Andela, N., Bi, J., Broquet, G., Canadell, J.G., Chevallier, F., Liu, Y.Y., Running, S.W., Sitch, S., van der Werf, G. R. (2014) Contribution of semi-arid ecosystems to interannual variability of the global carbon cycle. *Nature*, **509**, 600-603.

https://doi.org/10.1038/nature13376

70 71

72

73

74

75

76 77

78

79

80

81

82 83

84

85 86

87

88 89

90

91

92

93 94 95

96

97

98

99

00

01 02

03

04

05

06

07 80

09

10

11

12

13

14

15

16

17

18

19

6. Phillips, O.L., Aragão, L.E.O.C., Lewis, S.L., Fisher, J.B., Lloyd, J., López-González, G., Malhi, Y., Monteagudo, A., Peacock, J., Quesada, C.A., van der Heijden, G., Almeida, S., Amaral., I., Arrovo, L., Avmard, G., Baker, T.R., Banki, O., Blanc, L., Bonal, D., Brando, P., Chave, J., Oliveira, A. C.A., Cardozo, N.D., Czimczik, C.I., Feldpausch, T.R., Freitas, M.A., Gloor, E., Higuchi, N., Jiménez, E., Lloyd, G., Meir, P., Mendoza, C., Morel, A., Neill, D.A., Nepstad, D., Patiño, S., Peñuela, M.C., Prieto, A., Ramírez, F., Schwarz, M., Silva, J., Silveira, M., Thomas, A.S., Steege, H.T., Stropp, J., Vásquez, R., Zelazowski, P., Alvarez, D. E., Andelman, S., Andrade, A., Chao, K.J., Erwin, T., Di Fiore, A., Honorio, C. E., Keeling H, Killeen TJ, Laurance WF, Peña Cruz A, Pitman NC, Núñez Vargas P, Ramírez-Angulo, H., Rudas, A., Salamão, R., Silva, N., Terborgh, J., Torres-Lezama, A. (2009)

Drought Sensitivity of the Amazon Rainforest. Science (80-.)., 323, 1344 LP – 1347.

Science Advances Page 16 of 47

```
https://doi.org/10.1126/science.1164033
```

- 7. Lewis, S.L., Brando, P.M., Phillips, O.L., van der Heijden, G.M.F. and Nepstad, D. (2011) The 2010 Amazon Drought. *Science* (80-.)., **331**, 554 LP – 554.
- 24 https://doi.org/10.1126/science.1200807

- 8. Jiménez-Muñoz, J.C., Mattar, C., Barichivich, J., Santamaría-Artigas, A., Takahashi, K., Malhi, Y., Sobrino, J.A. and Schrier, G. van der (2016) Record-breaking warming and extreme drought in the Amazon rainforest during the course of El Niño 2015–2016. *Sci. Rep.*, 6, 33130.
 - https://doi.org/10.1038/srep33130

9. Bowman, K.W., Liu, J., Bloom, A.A., Parazoo, N.C., Lee, M., Jiang, Z., Menemenlis, D., Gierach, M.M., Collatz, G.J., Gurney, K.R., Wunch, D. (2017) Global and Brazilian Carbon Response to El Niño Modoki 2011–2010. *Earth Sp. Sci.*, 4. https://doi.org/10.1002/2016EA000204

10. Wang,J., Zeng,N., Wang,M., Jiang,F., Chevallier,F., Crowell,S., He,W., Johnson,M.S., Liu,J., Liu,Z., Miller,S.M., Philip,S., Wang,H., Wu, M., Ju,W., Feng,S., Jia, M., (2023) Anomalous Net Biome Exchange Over Amazonian Rainforests Induced by the 2015/16 El Niño: Soil Dryness-Shaped Spatial Pattern but Temperature-dominated Total Flux. *Geophys. Res. Lett.*, **50**, e2023GL103379. https://doi.org/https://doi.org/10.1029/2023GL103379

11. Liu, J., Bowman, K.W., Schimel, D.S., Parazoo, N.C., Jiang, Z., Lee, M., Bloom, A.A., Wunch, D., Frankenberg, C., Sun, Y., O'Dell, C. W., Gurney, K. R., Dimitris, M., Michelle, G., Crisp, D., Eldering, A. (2017) Contrasting carbon cycle responses of the tropical continents to the 2015–2016 El Niño. *Science* (80-.)., **358**. https://doi.org/10.1126/science.aam5690

12. Byrne,B., Liu,J., Lee,M., Yin,Y., Bowman,K.W., Miyazaki,K., Norton,A.J., Joiner,J., Pollard,D.F., Griffith,D.W.T., Velazco, V. A., Deutscher, N.M., Jones, N.B., Paton-Walsh, C. (2021) The Carbon Cycle of Southeast Australia During 2019–2020: Drought, Fires, and Subsequent Recovery. *AGU Adv.*, **2**, e2021AV000469. https://doi.org/https://doi.org/10.1029/2021AV000469

13. Peiro,H., Crowell,S., Schuh,A., Baker,D.F., O'Dell,C., Jacobson,A.R., Chevallier,F., Liu,J., Eldering,A., Crisp,D., Crisp, D., Deng, F., Weir, B., Basu, S., Johnson, M. S., Philip, S., and Baker, I. (2021) Four years of global carbon cycle observed from OCO-2 version 9 and in situ data, and comparison to OCO-2 v7. *Atmos. Chem. Phys. Discuss.*, **2021**, 1–50. https://doi.org/10.5194/acp-2021-373

Science Advances

14. Byrne,B., Baker,D.F., Basu,S., Bertolacci,M., Bowman,K.W., Carroll,D., Chatterjee,A., Chevallier,F., Ciais,P., Cressie,N., Crisp, D., Crowell, S., Deng, F., Deng, Z., Deutscher, N. M., Dubey, M. K., Feng, S., García, O. E., Griffith, D. W. T., Herkommer, B., Hu, L., Jacobson, A. R., Janardanan, R., Jeong, S., Johnson, M. S., Jones, D. B. A., Kivi, R., Liu, J., Liu, Z., Maksyutov, S., Miller, J. B., Miller, S. M., Morino, I., Notholt, J., Oda, T., O'Dell, C. W., Oh, Y.-S., Ohyama, H., Patra, P. K., Peiro, H., Petri, C., Philip, S., Pollard, D. F., Poulter, B., Remaud, M., Schuh, A., Sha, M. K., Shiomi, K., Strong, K., Sweeney, C., Té, Y., Tian, H., Velazco, V. A., Vrekoussis, M., Warneke, T., Worden, J. R., Wunch, D., Yao,

Page 17 of 47

Y., Yun, J., Zammit-Mangion, A., and Zeng, N. (2023) National CO2 budgets (2015--2020) inferred from atmospheric CO2 observations in support of the global stocktake. Earth Syst. Sci. Data, 15, 963–1004.

https://doi.org/10.5194/essd-15-963-2023

73 74 75

76

77

78

72

70 71

> 15. Jiang, F., Wang, H., Chen, J.M., Ju, W., Tian, X., Feng, S., Li, G., Chen, Z., Zhang, S., Lu, X., Liu, J., Wang, H., Wang, J., He, W., and Wu, M. (2021) Regional CO2 fluxes from 2010 to 2015 inferred from GOSAT XCO2 retrievals using a new version of the Global Carbon Assimilation System. Atmos. Chem. Phys., 21, 1963–1985. https://doi.org/10.5194/acp-21-1963-2021

79 80 81

82

83

84

16. He, W., Jiang, F., Ju, W., Byrne, B., Xiao, J., Nguyen, N.T., Wu, M., Wang, S., Wang, J., Rödenbeck, C., Li, X., Scholze, M., Monteil, G., Wang, H., Zhou, Y., He, Q., Chen, J.M. (2023) Do State-Of-The-Art Atmospheric CO2 Inverse Models Capture Drought Impacts on the European Land Carbon Uptake? J. Adv. Model. Earth Syst., 15, e2022MS003150. https://doi.org/https://doi.org/10.1029/2022MS003150

85 86 87

88

89

17. Gu, L., Baldocchi, D.D., Wofsy, S.C., Munger, J.W., Michalsky, J.J., Urbanski, S.P. and Boden, T.A. (2003) Response of a Deciduous Forest to the Mount Pinatubo Eruption: Enhanced Photosynthesis. Science (80-.)., 299, 2035–2038. https://doi.org/10.1126/science.1078366

90 91 92

93

18. Bosilovich, M.G., Robertson, F.R. and Stackhouse, P.W. (2020) El Niño-Related Tropical Land Surface Water and Energy Response in MERRA-2. J. Clim., 33, 1155–1176. https://doi.org/https://doi.org/10.1175/JCLI-D-19-0231.1

94 95 96

97

98

99 00

01

02

03

04

05

06

08

19. Friedlingstein, P., O'Sullivan, M., Jones, M.W., Andrew, R.M., Gregor, L., Hauck, J., Le Quéré, C., Luijkx, I.T., Olsen, A., Peters, G.P., Peters, W., Pongratz, J., Schwingshackl, C., Sitch, S., Canadell, J. G., Ciais, P., Jackson, R. B., Alin, S. R., Alkama, R., Arneth, A., Arora, V. K., Bates, N. R., Becker, M., Bellouin, N., Bittig, H. C., Bopp, L., Chevallier, F., Chini, L. P., Cronin, M., Evans, W., Falk, S., Feely, R. A., Gasser, T., Gehlen, M., Gkritzalis, T., Gloege, L., Grassi, G., Gruber, N., Gürses, Ö., Harris, I., Hefner, M., Houghton, R. A., Hurtt, G. C., Iida, Y., Ilyina, T., Jain, A. K., Jersild, A., Kadono, K., Kato, E., Kennedy, D., Klein Goldewijk, K., Knauer, J., Korsbakken, J. I., Landschützer, P., Lefèvre, N., Lindsay, K., Liu, J., Liu, Z., Marland, G., Mayot, N., McGrath, M. J., Metzl, N., Monacci, N. M., Munro, D. R., Nakaoka, S.-I., Niwa, Y., O'Brien, K., Ono, T., Palmer, P. I., Pan, N., Pierrot, D., Pocock, K., Poulter, B., Resplandy, L., Robertson, E., Rödenbeck, C., Rodriguez, C., Rosan, T. M., Schwinger, J., Séférian, R., Shutler, J. D., Skjelvan, I., Steinhoff, T., Sun, Q., Sutton, A. J., Sweeney, C., Takao, S., Tanhua, T., Tans, P. P., Tian, X., Tian, H., Tilbrook, B., Tsujino, H., Tubiello, F., van der Werf, G. R., Walker, A. P., Wanninkhof, R., Whitehead, C., Willstrand Wranne, A., Wright, R., Yuan, W., Yue, C.,

07

09 10

- Yue, X., Zaehle, S., Zeng, J., and Zheng, B. (2022) Global Carbon Budget 2022. Earth Syst. 11

Sci. Data, 14, 4811–4900. 12

13 https://doi.org/10.5194/essd-14-4811-2022

14 15

16

20. Rödenbeck, C., Houweling, S., Gloor, M. and Heimann, M. (2003) CO2 flux history 1982– 2001 inferred from atmospheric data using a global inversion of atmospheric transport.

Atmos. Chem. Phys., 3, 1919–1964. 17

https://doi.org/10.5194/acp-3-1919-2003

18 19

> Science Advances Page 18 of 47

- 21. Bousquet, P., Peylin, P., Ciais, P., Quéré, C. Le, Friedlingstein, P. and Tans, P.P. (2000) 20 21 Regional Changes in Carbon Dioxide Fluxes of Land and Oceans Since 1980. Science (80-.)., **290**, 1342–1346. 22
 - https://doi.org/10.1126/science.290.5495.1342

- 22. Baker, D.F., Law, R.M., Gurney, K.R., Rayner, P., Peylin, P., Denning, A.S., Bousquet, P., 25 Bruhwiler, L., Chen, Y.-H., Ciais, P., Fung, I.Y., Heimann, M., John, J., Maki, T., Maksyutov, 26 27 S., Masarie, K., Prather, M., Pak, B., Taguchi, S., Zhu, Z. (2006) TransCom 3 inversion intercomparison: Impact of transport model errors on the interannual variability of regional 28 CO2 fluxes, 1988–2003. Global Biogeochem. Cycles, 20. 29 30
 - https://doi.org/https://doi.org/10.1029/2004GB002439

31 32

23. Leamon, R.J. (2023) The triple-dip La Niña of 2020–22: updates to the correlation of ENSO with the termination of solar cycles. Front. Earth Sci., 11. https://doi.org/10.3389/feart.2023.1204191

34 35 36

37

33

24. Gao, C., Chen, M., Zhou, L., Feng, L. and Zhang, R.-H. (2022) The 2020–2021 prolonged La Niña evolution in the tropical Pacific. Sci. China Earth Sci., 65, 2248–2266. https://doi.org/10.1007/s11430-022-9985-4

38 39 40

41

42

43

44

25. Gaubert, B., Stephens, B.B., Basu, S., Chevallier, F., Deng, F., Kort, E.A., Patra, P.K., Peters, W., Rödenbeck, C., Saeki, T., Schimel, D., Van der Laan-Luijkx, I., Wofsy, S., and Yin, Y. (2018) Global atmospheric CO<sub&gt;2&lt;/sub&gt; inverse models converging on neutral tropical land exchange but diverging on fossil fuel and atmospheric growth rate. Biogeosciences Discuss., 10.5194/bg-2018-384. https://doi.org/10.5194/bg-2018-384

45 46 47

48

49

50

51

26. Stephens, B.B., Gurney, K.R., Tans, P.P., Sweeney, C., Peters, W., Bruhwiler, L., Ciais, P., Ramonet, M., Bousquet, P., Nakazawa, T., Aoki, S., Machida, t., Inoue, G., Vinnichenko, N., Lloyd, J., Jordan, A., Heimann, M., Shibistova, O., Langenfelds, R.L., Steele, L. P., Francey, R.J., Denning, A.S. (2007) Weak Northern and Strong Tropical Land Carbon Uptake from Vertical Profiles of Atmospheric CO<sub>2</sub> Science (80-.)., 316, 1732 LP - 1735. https://doi.org/10.1126/science.1137004

52 53 54

55

56

57

27. Schuh, A.E. and Jacobson, A.R. (2023) Uncertainty in parameterized convection remains a key obstacle for estimating surface fluxes of carbon dioxide. Atmos. Chem. Phys., 23, 6285-6297.

https://doi.org/10.5194/acp-23-6285-2023

58 59 60

61

62

63

28. Zheng, B., Ciais, P., Chevallier, F., Yang, H., Canadell, J.G., Chen, Y., van der Velde, I.R., Aben, I., Chuvieco, E., Davis, S.J., Deeter, M., Hong, C., Kong, Y., Li, H., Li, H., Lin, X., He, K., Zhang, Q. (2023) Record-high CO2 emissions from boreal fires in 2021. Science (80-.). **379**, 912–917.

https://doi.org/10.1126/science.ade0805

64 65

66 29. Bloom, A.A., Exbrayat, J., Velde, I.R. Van Der, Feng, L. and Williams, M. (2015) The decadal state of the terrestrial carbon cycle: Global retrievals of terrestrial carbon allocation, 67 pools, and residence times. 10.1073/pnas.1515160113. 68

https://doi.org/10.1073/pnas.1515160113 69

> Science Advances Page 19 of 47

- 30. Madani, N., Kimball, J.S., Parazoo, N.C., Ballantyne, A.P., Tagesson, T., Jones, L.A.,
- Reichle, R.H., Palmer, P.I., Velicogna, I., Bloom, A.A., Saatchi, S., Liu, Z., Geruo, A. (2020)
- Below-surface water mediates the response of African forests to reduced rainfall. *Environ*.
- 74 Res. Lett., **15**, 34063.
 - https://doi.org/10.1088/1748-9326/ab724a

31. Stocker,B.D., Tumber-Dávila,S.J., Konings,A.G., Anderson,M.C., Hain,C. and Jackson,R.B. (2023) Global patterns of water storage in the rooting zones of vegetation. *Nat. Geosci.*, **16**, 250–256.

80 https://doi.org/10.1038/s41561-023-01125-2

32. Fan, Y., Miguez-Macho, G., Jobbágy, E.G., Jackson, R.B. and Otero-Casal, C. (2017) Hydrologic regulation of plant rooting depth. *Proc. Natl. Acad. Sci.*, **114**, 10572 LP – 10577. https://doi.org/10.1073/pnas.1712381114

33. Zhou, T., Zhang, W., Zhang, L., Clark, R., Qian, C., Zhang, Q., Qiu, H., Jiang, J. and Zhang, X. (2022) 2021: A Year of Unprecedented Climate Extremes in Eastern Asia, North America, and Europe. *Adv. Atmos. Sci.*, **39**, 1598–1607. https://doi.org/10.1007/s00376-022-2063-9

34. Bastos, A., Janssens, I.A., Gouveia, C.M., Trigo, R.M., Ciais, P., Chevallier, F., Peñuelas, J., Rödenbeck, C., Piao, S., Friedlingstein, P., Running, S. W. (2016) European land CO2 sink influenced by NAO and East-Atlantic Pattern coupling. *Nat. Commun.*, 7, 10315. https://doi.org/10.1038/ncomms10315

35. Wang,J., Wang,M., Kim,J.-S., Joiner,J., Zeng,N., Jiang,F., Wang,H., He,W., Wu,M., Chen,T., Ju, W., Chen, J. M. (2021) Modulation of Land Photosynthesis by the Indian Ocean Dipole: Satellite-Based Observations and CMIP6 Future Projections. *Earth's Futur.*, **9**, e2020EF001942.

https://doi.org/https://doi.org/10.1029/2020EF001942

36. Kim, J.-S., Kug, J.-S., Jeong, S.-J., Park, H. and Schaepman-Strub, G. (2020) Extensive fires in southeastern Siberian permafrost linked to preceding Arctic Oscillation. *Sci. Adv.*, **6**, eaax3308.

https://doi.org/10.1126/sciadv.aax3308

37. Andres,R.J., Boden,T.A. and Higdon,D.M. (2016) Gridded uncertainty in fossil fuel carbon dioxide\hack{\newline} emission maps, a CDIAC example. *Atmos. Chem. Phys.*, **16**, 14979–14995.

https://doi.org/10.5194/acp-16-14979-2016

- 38. Ballantyne, A.P., Andres, R., Houghton, R., Stocker, B.D., Wanninkhof, R., Anderegg, W., Cooper, L.A., DeGrandpre, M., Tans, P.P., Miller, J.B., Alden, C., and White, J. W. C. (2015)
- Audit of the global carbon budget: estimate errors and their impact on uptake uncertainty.
- *Biogeosciences*, **12**, 2565–2584.
 - https://doi.org/10.5194/bg-12-2565-2015

39. Cox,P.M., Pearson,D., Booth,B.B., Friedlingstein,P., Huntingford,C., Jones,C.D. and Luke,C.M. (2013) constrained by carbon dioxide variability. *Nature*, **494**, 1–5.

Science Advances Page 20 of 47

40. Barkhordarian Kevin W and Cressie, Noel and Jewell, Jeffrey and Liu, Junjie, A. and B. (2021) Emergent constraints on tropical atmospheric aridity-carbon feedbacks and the future of carbon sequestration. Environ. Res. Lett.

24 25 26

27

28

29

23

41. Cai, W., Wang, G., Santoso, A., McPhaden, M.J., Wu, L., Jin, F.-F., Timmermann, A., Collins, M., Vecchi, G., Lengaigne, M., England, M.H., Dommenget, D., Takahashi, K., Guilyardi, E. (2015) Increased frequency of extreme La Niña events under greenhouse warming. Nat. Clim. Chang., 5, 132–137. https://doi.org/10.1038/nclimate2492

30 31 32

42. Basu, S. and Nassar, R. (2023) Fossil Fuel CO# Emissions for the OCO2 Model Intercomparison Project (MIP). 10.5281/zenodo.8325420. https://doi.org/10.5281/zenodo.8325420

34 35 36

37

38 39

40

41

42

43

44

45

33

43. Le Quéré, C., Andrew, R.M., Friedlingstein, P., Sitch, S., Pongratz, J., Manning, A.C., Korsbakken, J.I., Peters, G.P., Canadell, J.G., Jackson, R.B., Boden, T. A., Tans, P. P., Andrews, O. D., Arora, V. K., Bakker, D. C. E., Barbero, L., Becker, M., Betts, R. A., Bopp, L., Chevallier, F., Chini, L. P., Ciais, P., Cosca, C. E., Cross, J., Currie, K., Gasser, T., Harris, I., Hauck, J., Haverd, V., Houghton, R. A., Hunt, C. W., Hurtt, G., Ilyina, T., Jain, A. K., Kato, E., Kautz, M., Keeling, R. F., Klein Goldewijk, K., Körtzinger, A., Landschützer, P., Lefèvre, N., Lenton, A., Lienert, S., Lima, I., Lombardozzi, D., Metzl, N., Millero, F., Monteiro, P. M. S., Munro, D. R., Nabel, J. E. M. S., Nakaoka, S., Nojiri, Y., Padin, X. A., Peregon, A., Pfeil, B., Pierrot, D., Poulter, B., Rehder, G., Reimer, J., Rödenbeck, C., Schwinger, J., Séférian, R., Skjelvan, I., Stocker, B. D., Tian, H., Tilbrook, B., Tubiello, F. N., van der Laan-Luijkx, I. T., van der Werf, G. R., van Heuven, S., Viovy, N., Vuichard, N., Walker, A. P., Watson, A. J., Wiltshire, A. J., Zaehle, S., and Zhu, D.: (2018) Global Carbon

46 47

Budget 2017. Earth Syst. Sci. Data, 10, 405-448.

48 49

https://doi.org/10.5194/essd-10-405-2018

50 51

52

53

54 55 44. Davis, K.J., Obland, M.D., Lin, B., Lauvaux, T., O'Dell, C., Meadows, B., Browell, E. V. DiGangi, J.P., Sweeney, C., McGill, Barrick, M.J., Nehrir, A.R., Yang, M.M., Bennett, J.R., Baier, B.C., Roiger, A. Pal, S., Gerken, T., Fried, A., Feng, S., Shrestha, R., Shook, M.A., Chen, G., Campbell, L.J., Barkley, Z.R., and Pauly, R.M. (2018) ACT-America: L3 Merged In Situ Atmospheric Trace Gases and Flask Data, Eastern USA. 10.3334/ORNLDAAC/1593.

56

https://doi.org/10.3334/ORNLDAAC/1593 57

58 59

60

61

62

63

64

65

67

45. Wei, Y., Shrestha, R., Pal, S., Gerken, T., Feng, S., McNelis, J., Singh, D., Thornton, M.M., Boyer, A.G., Shook, M.A., Chen, G., Baier, B. C., Barkley, Z.R., Barrick, J. D., Bennett, J. R., Browell, E. V., Campbell, J. F., Campbell, L. J., Choi, Y., Collins, J., Dobler, J., Eckl, M., Fiehn, A., Fried, A., Digangi, J. P., Barton-Grimley, R., Halliday, H., Klausner, T., Kooi, S., Kostinek, J., Lauvaux, T., Lin, B., McGill, M.J., Meadows, B., Miles, N. L., Nehrir, A. R., Nowak, J. B., Obland, M., O'Dell, C., Fao, R. M.P., Richardson, S. J., Richter, D., Roiger, A., Sweeney, C., Walega, J., Weibring, P., Williams, C. A., Yang, M.M., Zhou, Y., Davis, K. J. (2021) Atmospheric Carbon and Transport – America (ACT-America) Data

66

Sets: Description, Management, and Delivery. Earth Sp. Sci., 8, e2020EA001634.

https://doi.org/https://doi.org/10.1029/2020EA001634 68

69

Science Advances Page 21 of 47 46. Davis, K.J., Browell, E. V, Feng, S., Lauvaux, T., Obland, M.D., Pal, S., Baier, B.C.,
Baker, D.F., Baker, I.T., Barkley, Z.R., Bowman, K., Cui, Y., Denning, A. S., DiGangi, J.P.,
Dobler, J.T., Fried, A., Gerken, T., Keller, K., Lin, B., Nehrir, A.R., Normile, C.P., O'Dell,
C.W., Ott, L.E., Roiger, A., Schuh, A.E., Sweeney, C., Wei, Y., Weir, B., Xue, M.,
Williams, C. A. (2021) The Atmospheric Carbon and Transport (ACT)-America Mission.
Bull. Am. Meteorol. Soc., 102, E1714–E1734.
https://doi.org/10.1175/BAMS-D-20-0300.1

47. Baier,B.C., Sweeney,C., Choi,Y., Davis,K.J., DiGangi,J.P., Feng,S., Fried,A., Halliday,H., Higgs,J., Lauvaux,T., Miller, B.R., Montzka, S. A., Newberger, T., Nowak, J. B., Patra, P., Richter, D., Walega, J., Weibring, P. (2020) Multispecies Assessment of Factors Influencing Regional CO2 and CH4 Enhancements During the Winter 2017 ACT-America Campaign. *J. Geophys. Res. Atmos.*, **125**, e2019JD031339. https://doi.org/https://doi.org/10.1029/2019JD031339

48. Machida, T., Matsueda, H., Sawa, Y., Nakagawa, Y., Hirotani, K., Kondo, N., Goto, K., Nakazawa, T., Ishikawa, K. and Ogawa, T. (2008) Worldwide Measurements of Atmospheric CO2 and Other Trace Gas Species Using Commercial Airlines. *J. Atmos. Ocean. Technol.*, **25**, 1744–1754.

https://doi.org/10.1175/2008JTECHA1082.1

49. Joiner, J. and Yoshida, Y. (2020) Agricultural and Forest Meteorology Satellite-based re fl ectances capture large fraction of variability in global gross primary production (GPP) at weekly time scales. **291**.

https://doi.org/10.1016/j.agrformet.2020.108092

50. Li,X. and Xiao,J. (2019) Mapping Photosynthesis Solely from Solar-Induced Chlorophyll Fluorescence: A Global, Fine-Resolution Dataset of Gross Primary Production Derived from OCO-2. *Remote Sens.*, **11**. https://doi.org/10.3390/rs11212563

51. Zheng,B. (2022) Global fire CO2 emissions 2000-2021. 10.6084/m9.figshare.21770624.v1. https://doi.org/10.6084/m9.figshare.21770624.v1

52. Yue, C., Ciais, P., Houghton, R.A. and Nassikas, A.A. (2020) Contribution of land use to the interannual variability of the land carbon cycle. *Nat. Commun.*, **11**, 3170. https://doi.org/10.1038/s41467-020-16953-8

53. Eyring, V., Bony, S., Meehl, G.A., Senior, C.A., Stevens, B., Stouffer, R.J. and Taylor, K.E. (2016) Overview of the Coupled Model Intercomparison Project Phase 6 (CMIP6) experimental design and organization. *Geosci. Model Dev.*, **9**, 1937–1958. https://doi.org/10.5194/gmd-9-1937-2016

Acknowledgments

Funding:

Part of the research was carried out at the Jet Propulsion Laboratory, California Institute of Technology, under a contract with the National Aeronautics and Space Administration, (80NM0018D0004). LY was supported by the National Science Foundation (NSF)

(80NM0018D0004). J.X. was supported by the National Science Foundation (NSF)

(Macrosystem Biology & NEON-Enabled Science program: DEB-2017870). S. M.
acknowledges the NASA funding support 80NSSC21K1073. F.C. would like to
acknowledge the funding support from Copernicus Atmosphere Monitoring Service,
implemented by ECMWF on behalf of the European Commission (Grant: CAMS2 55 bis).
and the HPC resources of TGCC under the allocation A0130102201 made by GENCI.
M.S.J. acknowledges the internal funding from NASA's Earth Science Research and
Analysis Program.

Author contributions:

Conceptualization: JL

Methodology: JL, DB, SB, KB, BB, FC, WH, FJ, MSJ, TLK, XL, ZL, SMM, SP, JX, NZ

Investigation: JL, DB, SB, KB, BB, FC, WH, FJ, MSJ, XL, ZL, SMM, SP, JX, NZ Visualization: JL and JY

Writing—original draft: JL

Writing—review & editing: all co-authors contributed to reviewing and editing.

Competing interests: All other authors declare they have no competing interests.

Data and materials availability: All data are available in the main text or the supplementary materials. All the data sources are listed in Table S2 and publicly available.

29

30

31

32

3334

35

3637

38 39 40

Science Advances Page 23 of 47



Supplementary Materials for The reduced net carbon uptake over northern hemisphere land causes the close-to-normal CO2 growth rate in 2021 La Niña Junjie Liu* et al. *Corresponding author. Email: junjie.liu@jpl.nasa.gov This PDF file includes: Figs. S1 to S21 Tables S1 to S2 Reference 1-1

Science Advances Page 24 of 47

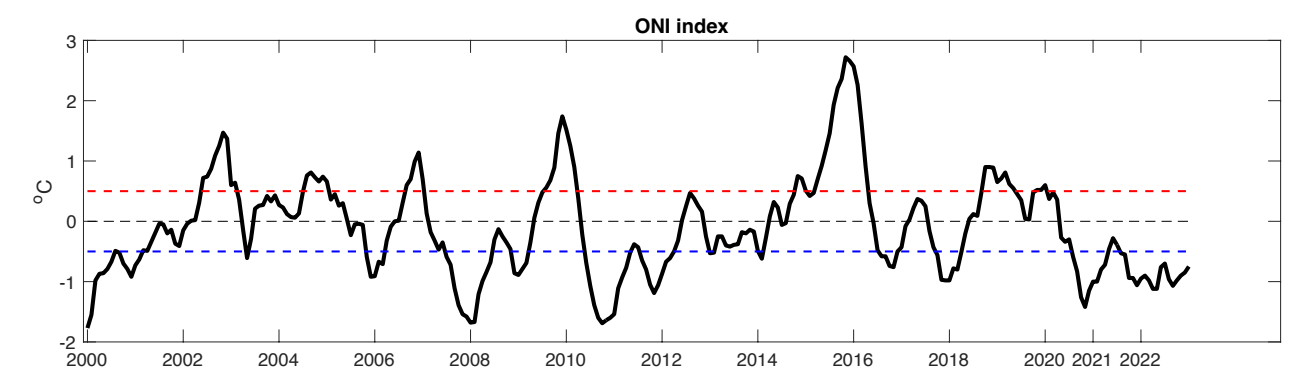


Fig. S1. Monthly ONI index between Jan 2000- Jan 2023 (unit: °C). It is defined as monthly running mean sea surface temperature (SST) anomalies in the Niño 3.4 region (5°N-5°S, 120°-170°W). When ONI index is lower than -0.5°C, it is defined as La Niña, and it is El Niño when ONI index is higher than 0.5°C. 2021 is in the middle of the longest La Niña in this century.

Science Advances Page 25 of 47

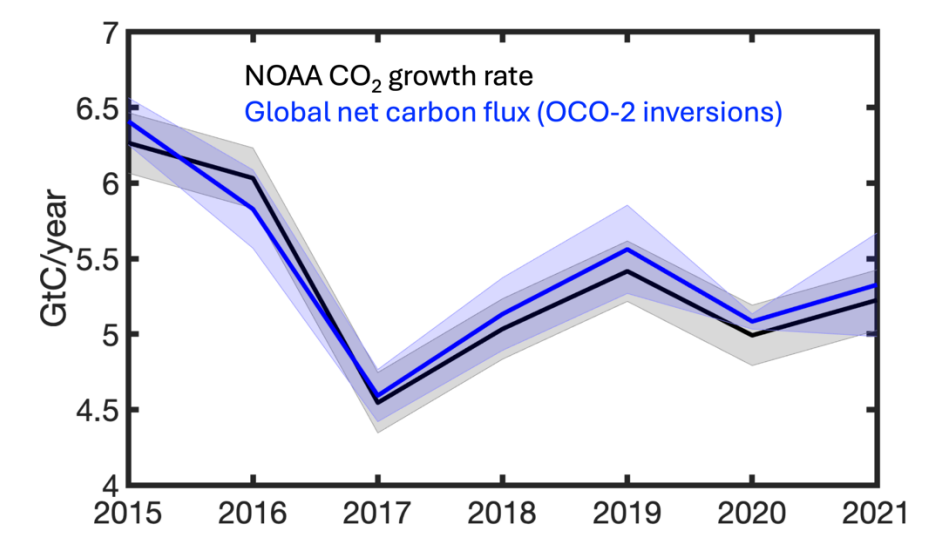


Figure S2 Comparison between NOAA global CO2 growth rate and the annual net carbon flux based on the ensemble OCO-2 inversions. The annual net carbon fluxes were calculated as the sum of fossil fuel emissions and natural carbon fluxes over land and ocean, which represent the total changes of atmospheric CO2 estimated by inversion models. The NOAA global CO2 growth rate was converted to gigaton carbon per year using the conversion factor of 2.124GtC/ppm (43). We assumed 0.2 GtC/year uncertainty for the observed NOAA annual CO2 growth following (19), while the ensemble model spread was used as the uncertainty for the inversion results.

Science Advances Page 26 of 47

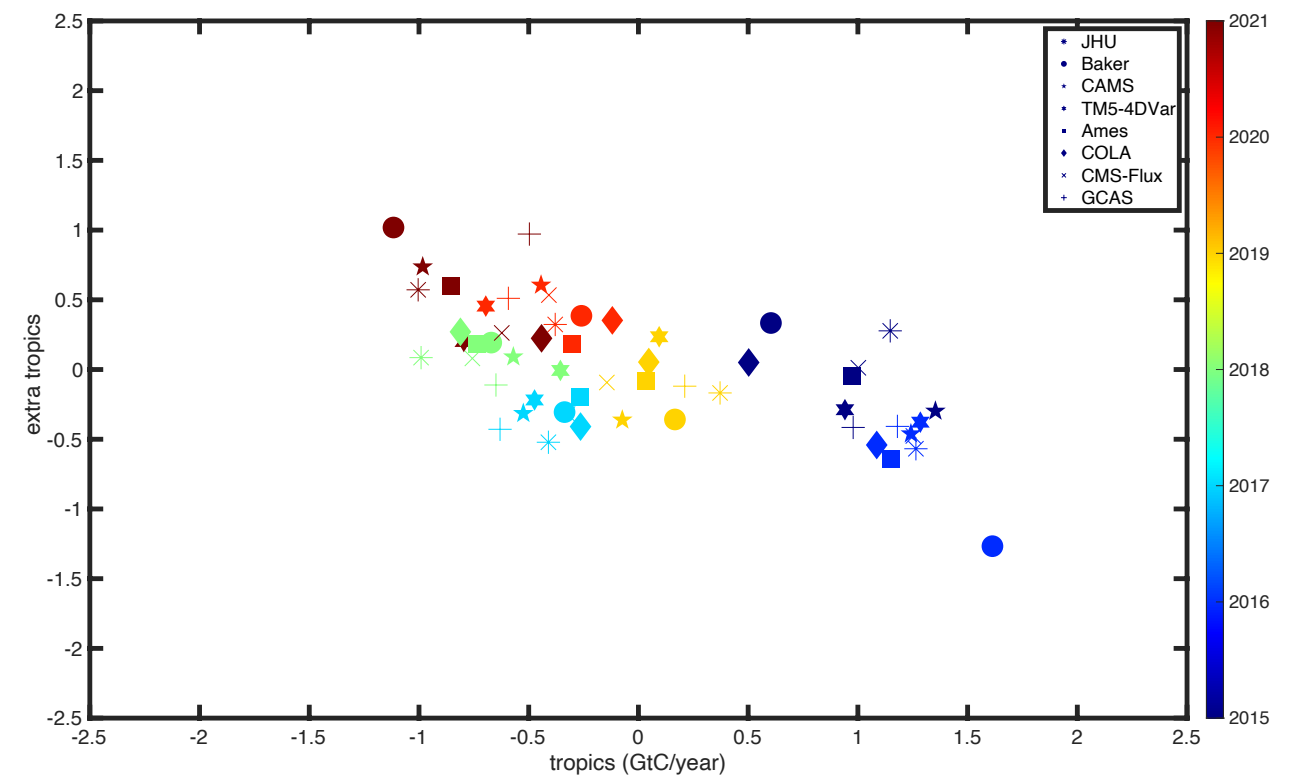


Figure S3 The annual net biosphere exchange (NBE) anomalies over the tropics and extra-tropics estimated by the eight inversion models, which are JHU, Baker, CAMS, TM5-4DVar, AMES, COLA, CMS-Flux, and GCAS. The color represents years. Unit: GtC/year.

Science Advances Page 27 of 47

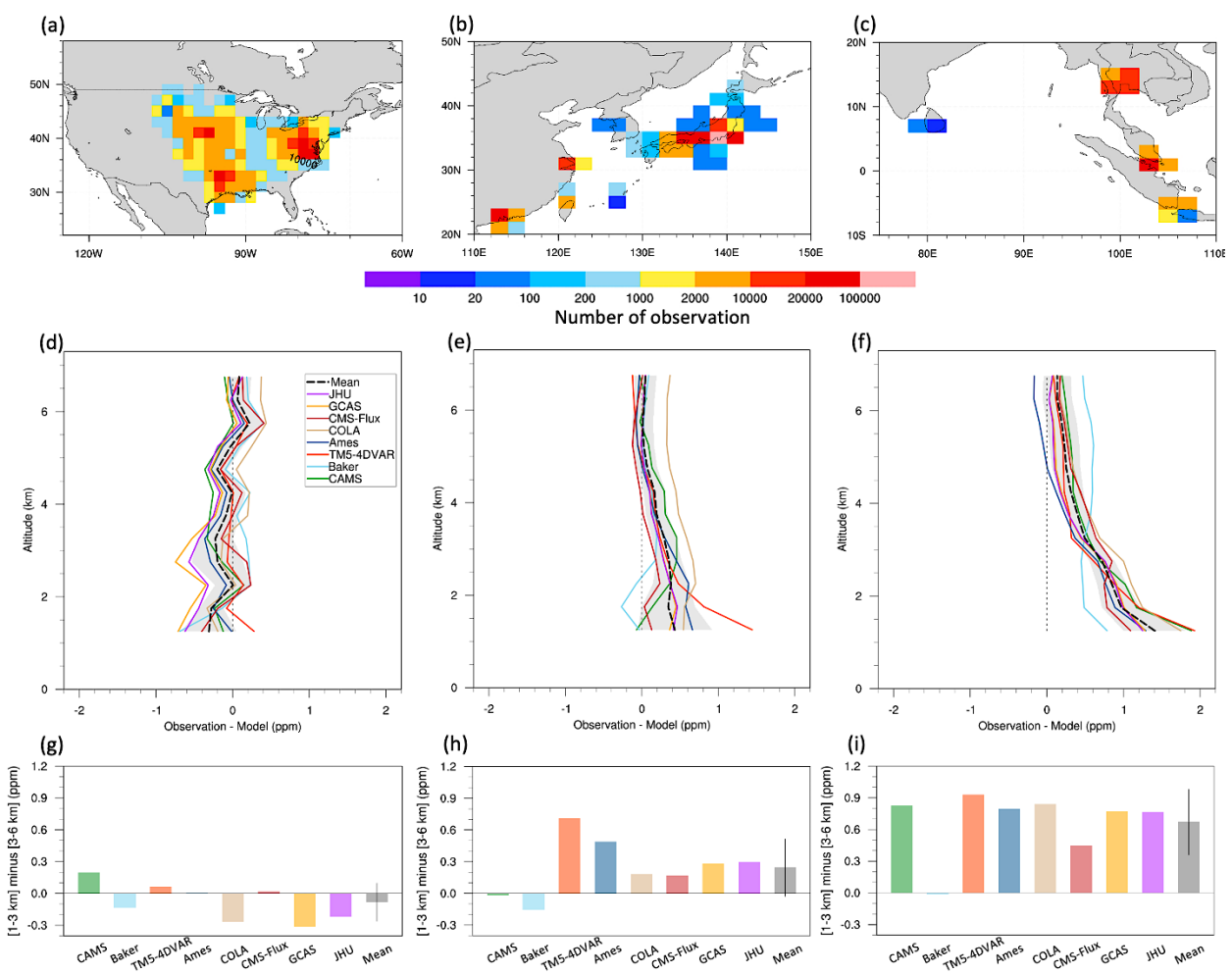


Figure S4 Spatial distributions of the number of aircraft atmospheric CO₂ observations from 1 km to 7 km over midlatitude North America (a), East Asia (b), and Southeast Asia (c) for the period 2015-2019. The aircraft observations are from the Atmospheric Carbon and Transport (ACT) – America and Comprehensive Observation Network for TRace gases by AIrLiner (CONTRAIL) projects (47). (d-f) Mean atmospheric CO₂ differences with a 0.5 km interval between observations and OCO-2 MIP models over each region for the same period. Black line and shaded area denote ensemble mean and one inter-model standard deviation range. (g-i) Vertical gradients of mean observation-model differences of atmospheric CO₂ for altitude ranges of 1-3 km and 3-6 km above ground.

Science Advances Page 28 of 47

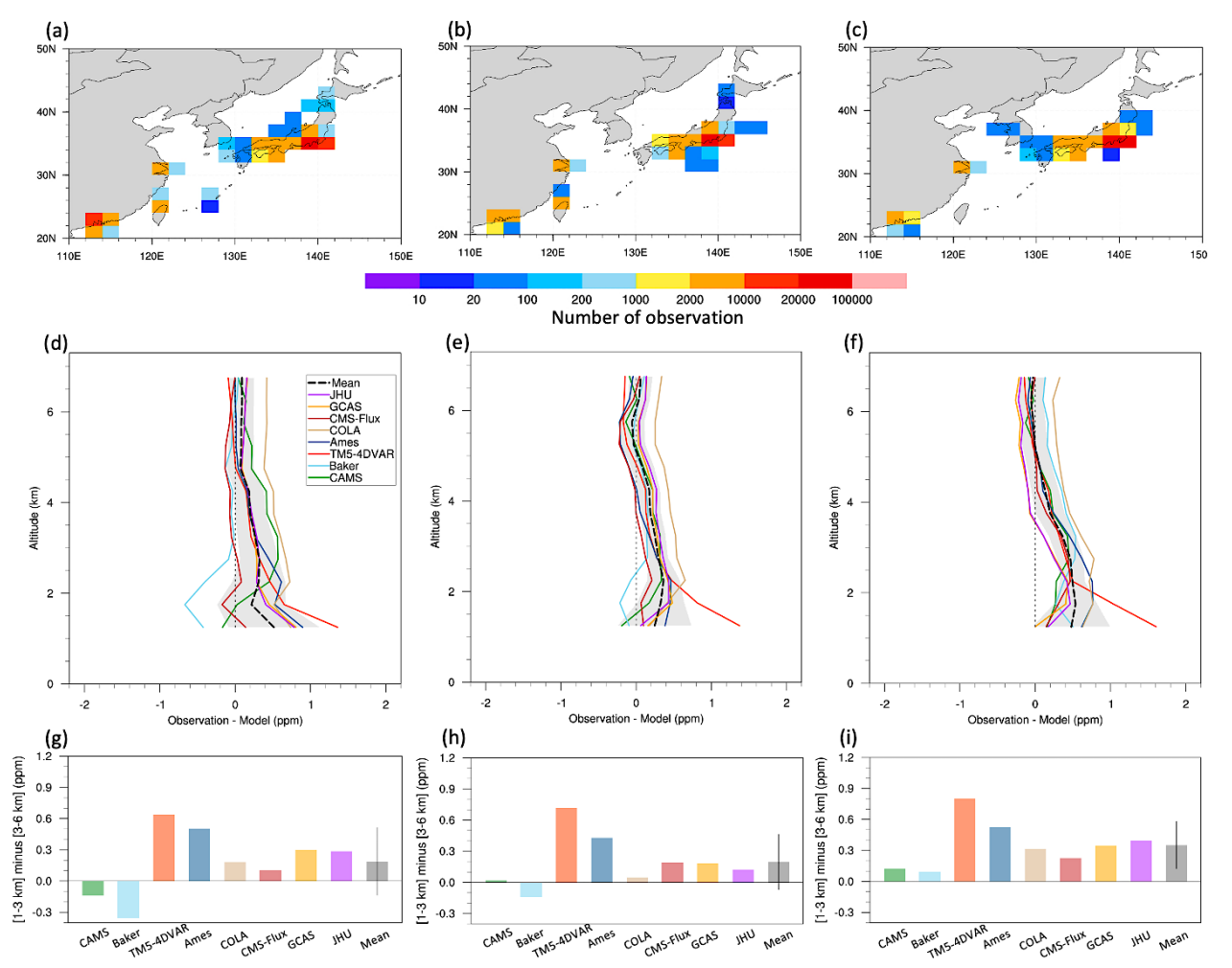


Figure S5 Same as Figure S4 but for aircraft atmospheric CO₂ observations over East Asia for 2015, 2016, and 2017.

Science Advances Page 29 of 47

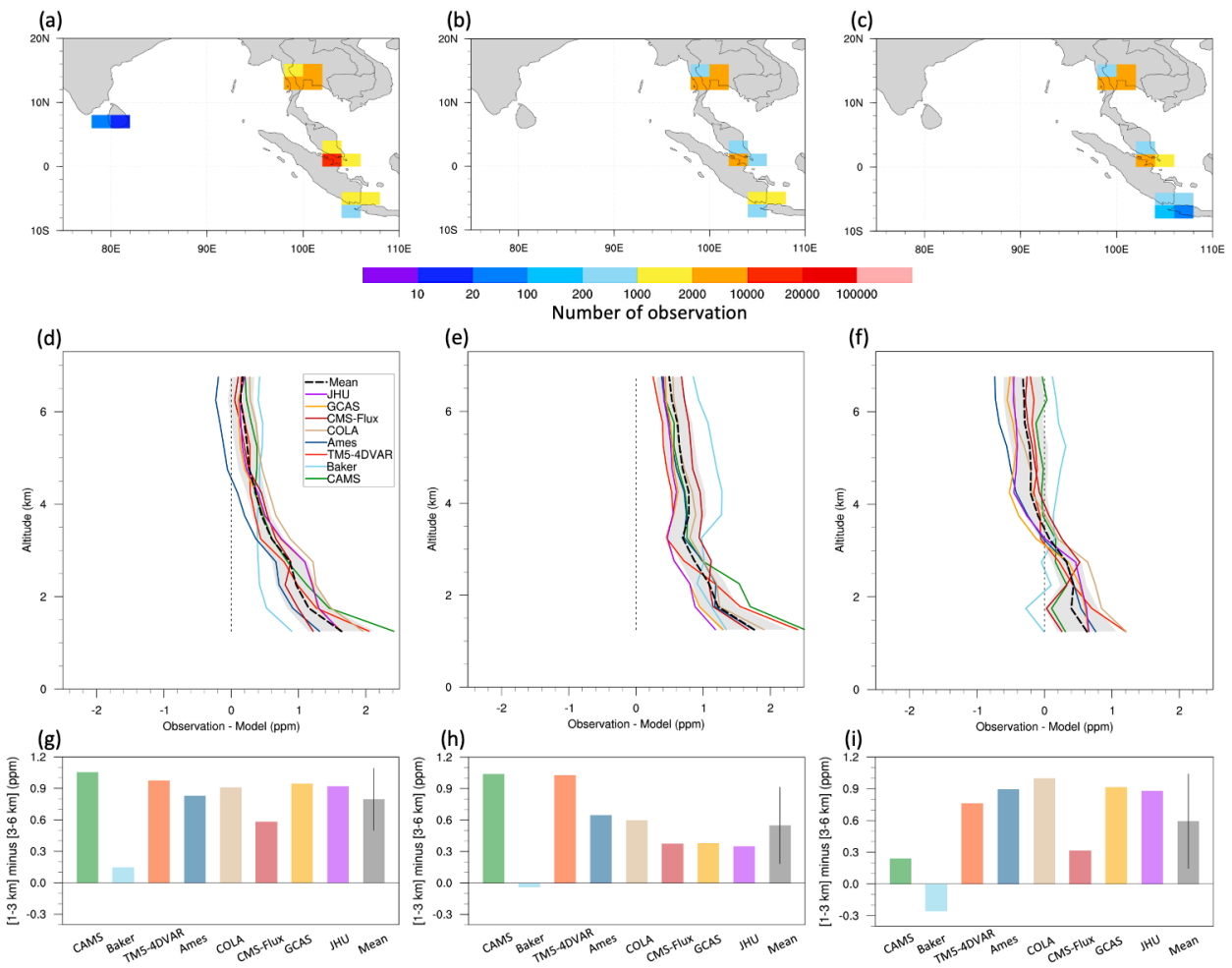
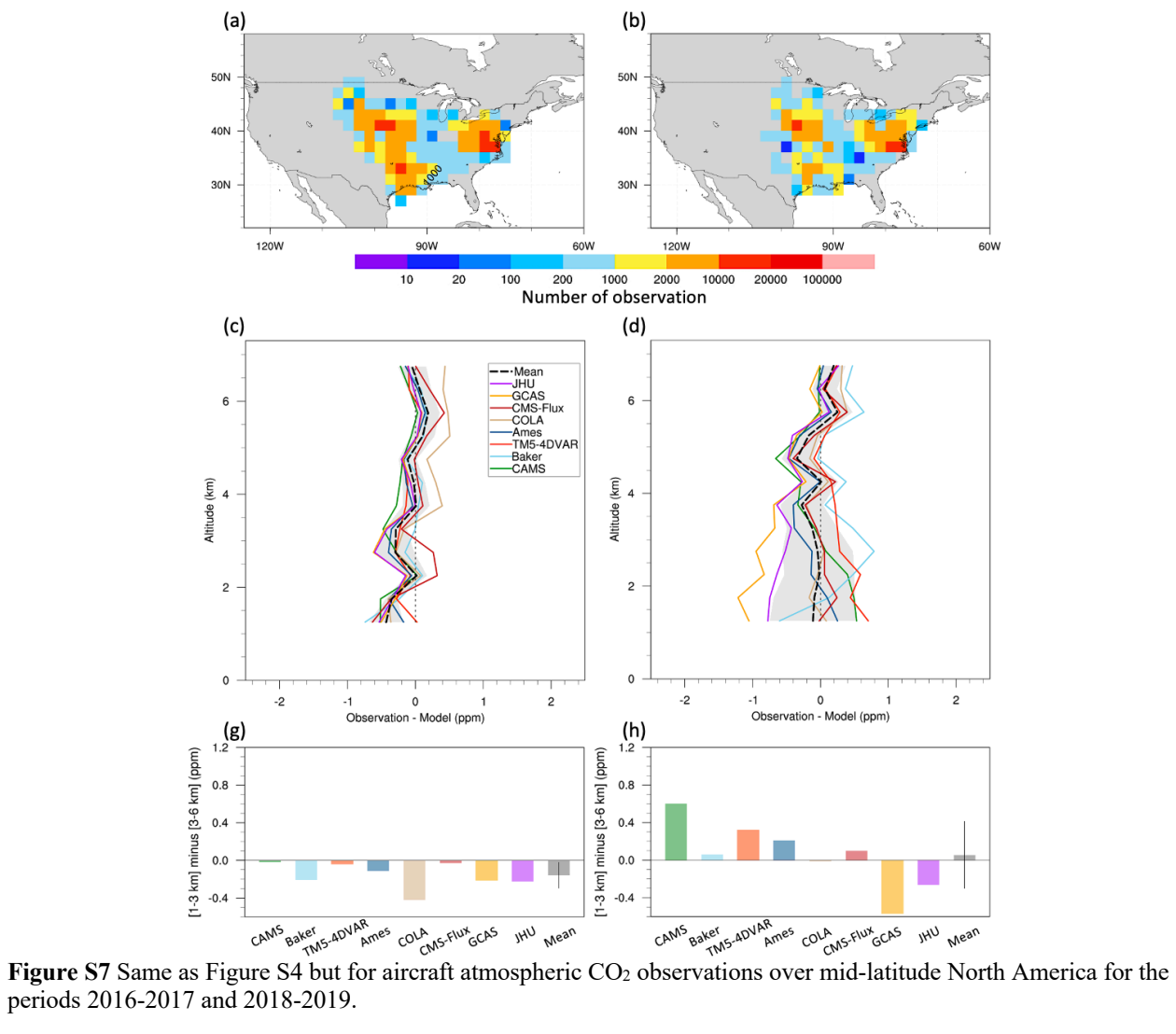


Figure S6 Same as Figure S4 but for aircraft atmospheric CO₂ observations over Southeast Asia for 2015, 2016, and 2017.

Science Advances Page 30 of 47



Science Advances Page 31 of 47

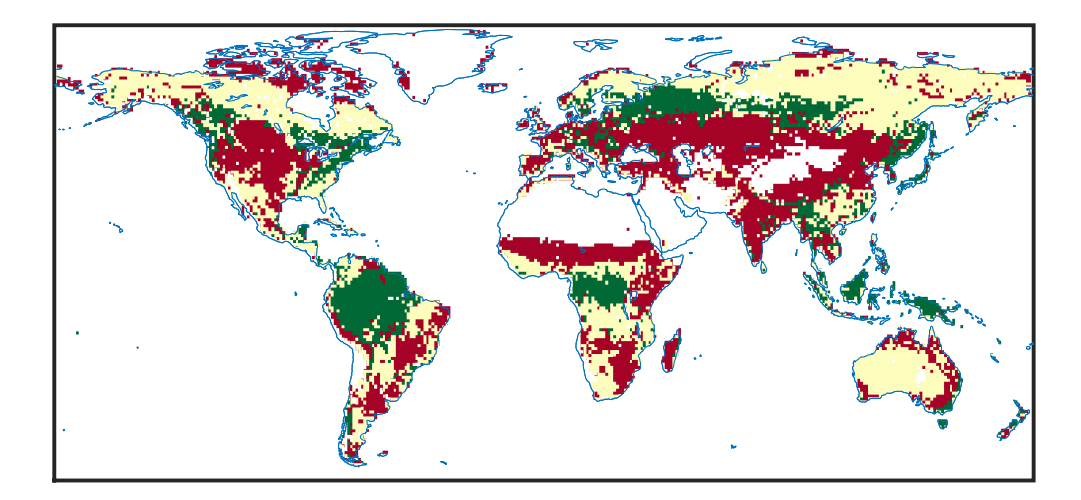


Fig. S8 Land cover classification based on MODIS IGBP 2020 data. Green: forest; yellow: semi-arid region; and red: grassland and cropland. Forest type includes evergreen needleleaf forest, evergreen broadleaf forest, deciduous needleleaf forest, deciduous broadleaf forest and mixed forest. Semiarid region includes grid points dominated by closed shrublands, open shrublands, woody savannas, and savannas.

Science Advances Page 32 of 47

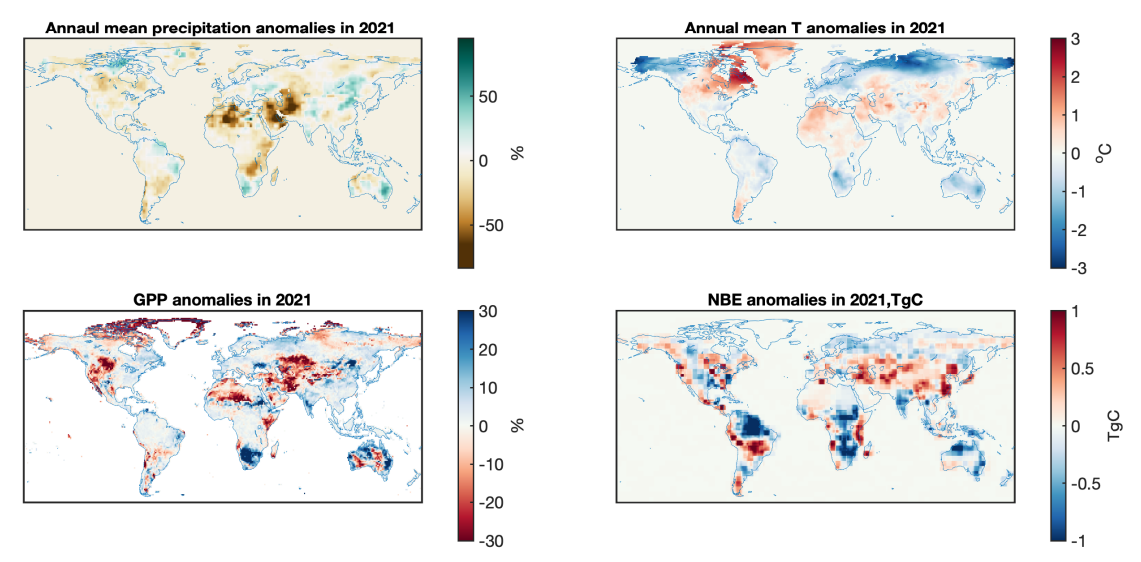


Fig. S9 Spatial distributions of annual climate and carbon flux anomalies. Top left. Percentage of annual precipitation anomalies (unit: %); top right annual temperature anomalies (unit: °C); bottom left: percentage of GPP anomalies (unit: %); bottom right: annual anomalies of net biosphere exchange (unit: tera grams of carbon; TgC).

Science Advances Page 33 of 47

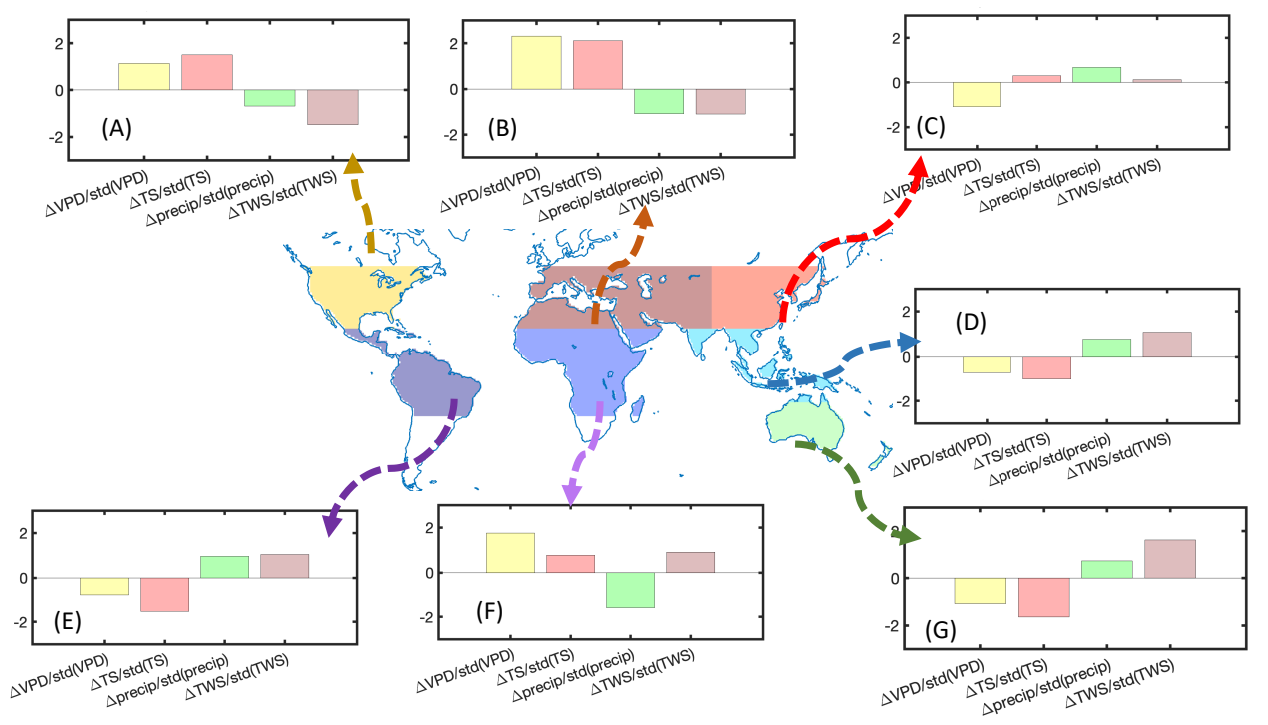


Figure S10 Regional normalized climate anomalies. Normalized annual anomalies of vapor pressure deficit (VPD) (yellow), surface temperature (Ts) (red), precipitation (green), and total water storage anomalies (brown) over mid latitudes of North America (NA) (A), Eurasia (B), East Asia (C), tropical Asia (D), rest of Australia (G), tropical Africa (F), and tropical South America (E) (clockwise). The normalized anomalies are defined as the ratio between annual anomalies in 2021 and standard deviation of annual anomalies over 2015-2021. For TWS, the standard deviation was calculated over 2015-2016 and 2019-2021 due to missing data in 2017 and 2018.

Science Advances Page 34 of 47

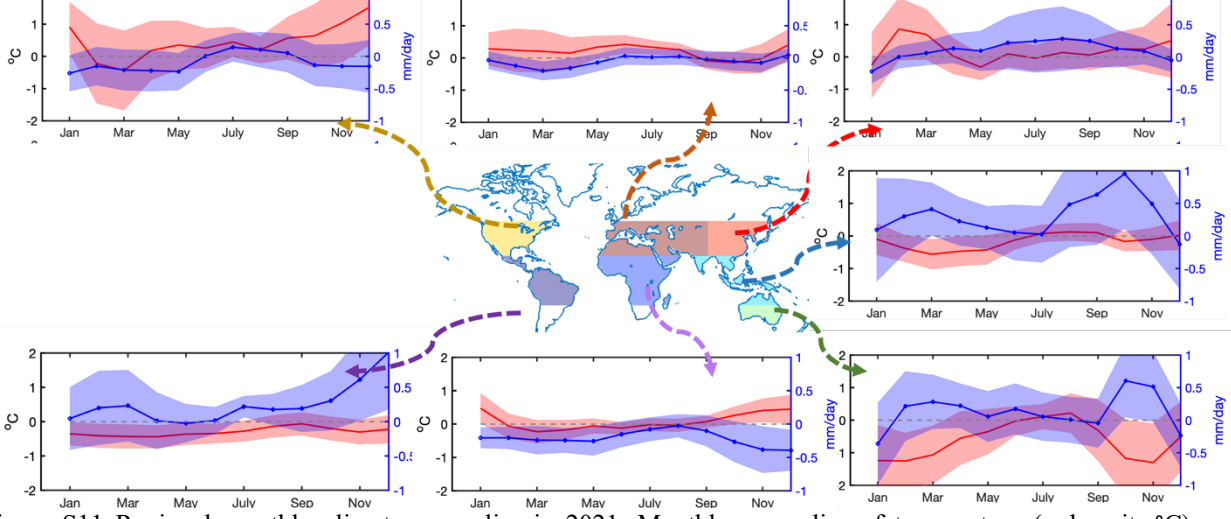
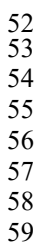


Figure S11 Regional monthly climate anomalies in 2021. Monthly anomalies of temperature (red, unit: °C) and precipitation (blue, unit: mm/day) over mid latitudes of North America (NA), Eurasia, East Asia, tropical Asia, the rest of Australia, tropical Africa, and tropical South America (clockwise). The shaded area represents monthly variations of regional mean temperature or precipitation between 2015-2021.

Science Advances
Page 35 of 47



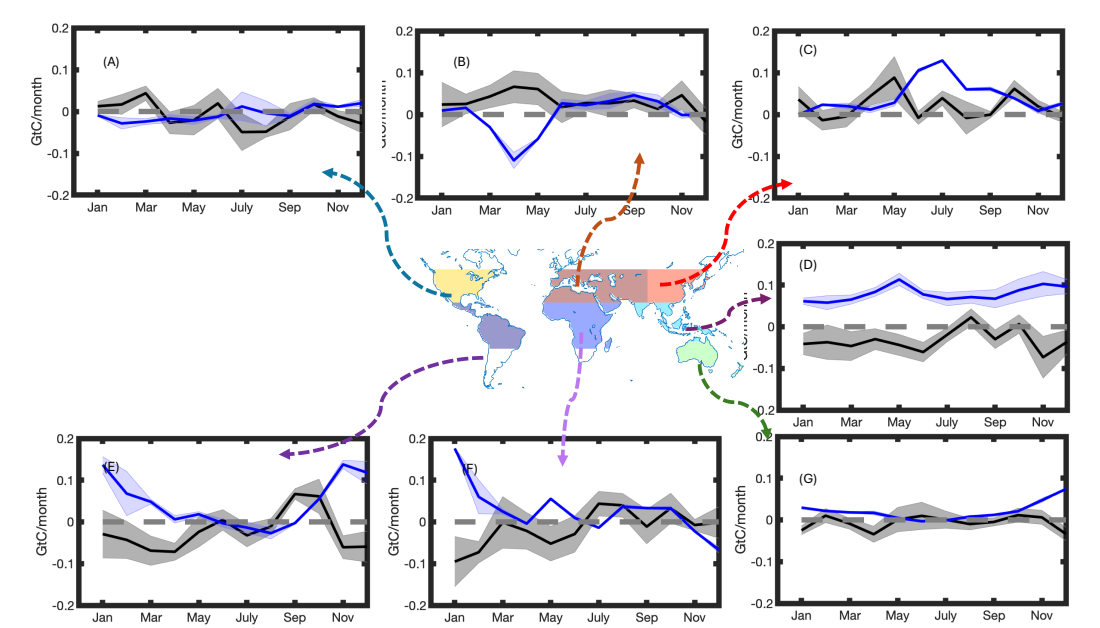


Figure S12 Regional monthly carbon flux anomalies in 2021. Monthly anomalies of GPP (blue, unit: GtC/month) and NBE (black, unit: GtC/month) over mid latitudes of North America (NA), Eurasia, East Asia, tropical Asia, the rest of Australia, tropical Africa, and tropical South America (clockwise).

Science Advances Page 36 of 47

 $\begin{array}{c} 61 \\ 62 \end{array}$

63

64

65

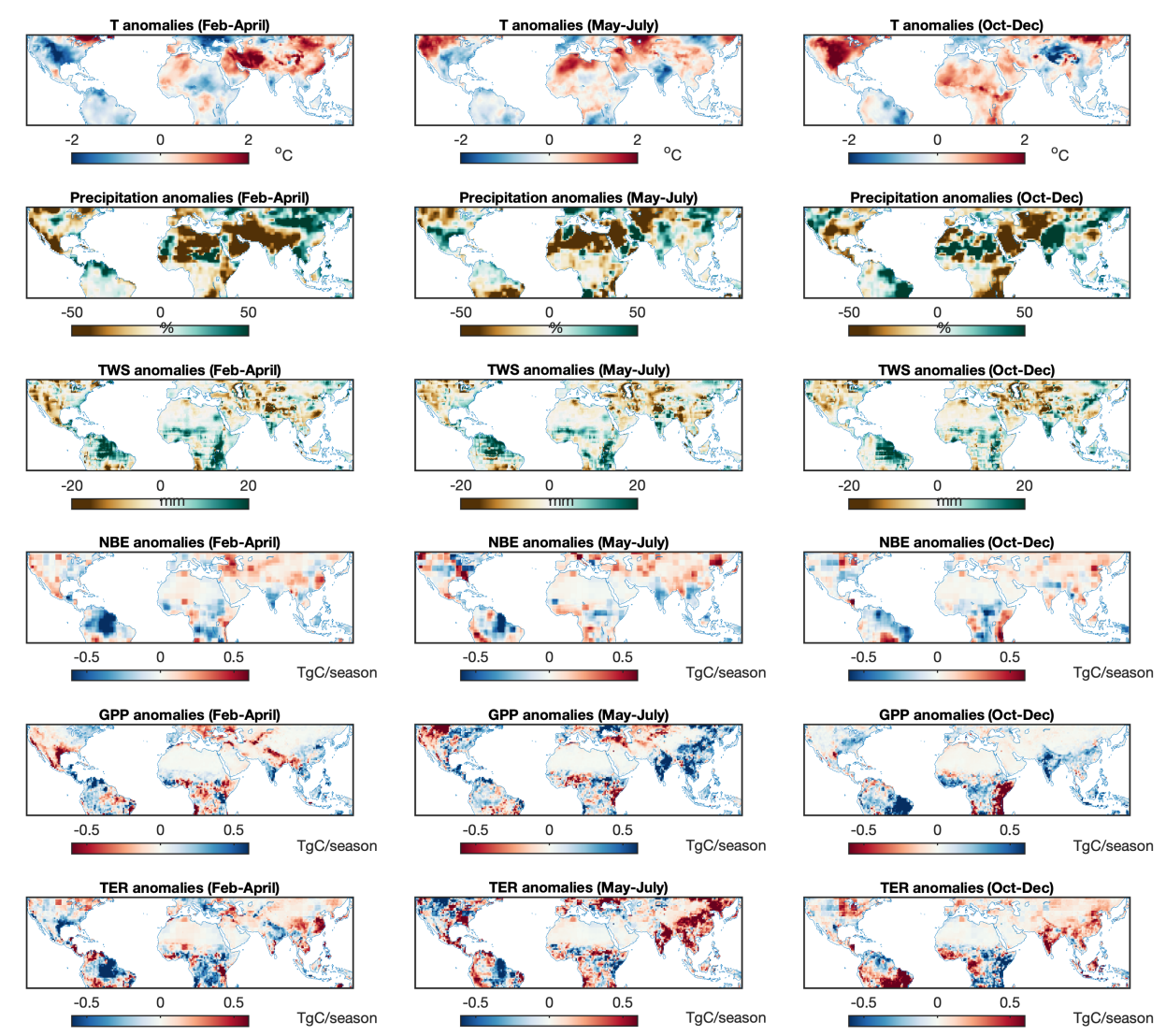


Figure S13 Temperature (top row), precipitation (second row), total water storage deficit (third row), NBE (fourth row), GPP (fifth row), and TER (sixth row) anomalies over Feb-April (left column), May-July (middle column), and Oct-Dec (right column) in 2021.

Science Advances Page 37 of 47

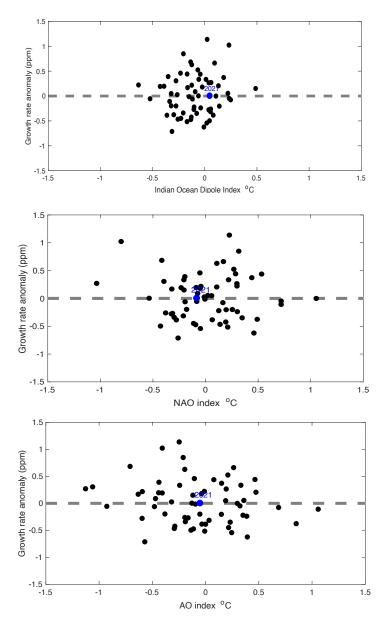


Figure S14 Top panel: annual mean Indian Ocean Dipole (IOD) Index vs. CO₂ growth rate anomaly between 1959-2021 without 1991 and 1992, when Pinatubo volcano eruption had a dominant impact. The Indian Ocean Dipole index data was downloaded from https://psl.noaa.gov/gcos_wgsp/Timeseries/DMI/. Middle panel: annual mean North Atlantic Oscillation (NAO) Index vs. CO₂ growth rate anomaly between 1959-2021 without 1991 and 1992. The NAO index data was downloaded from https://www.cpc.ncep.noaa.gov/products/precip/CWlink/pna/nao.shtml. Bottom panel: annual mean Arctic Oscillation (AO) Index vs. CO₂ growth rate anomaly between 1959-2021 without 1991 and 1992. The AO index data was downloaded from https://www.cpc.ncep.noaa.gov/products/precip/CWlink/daily_ao_index/ao.shtml.

Science Advances Page 38 of 47

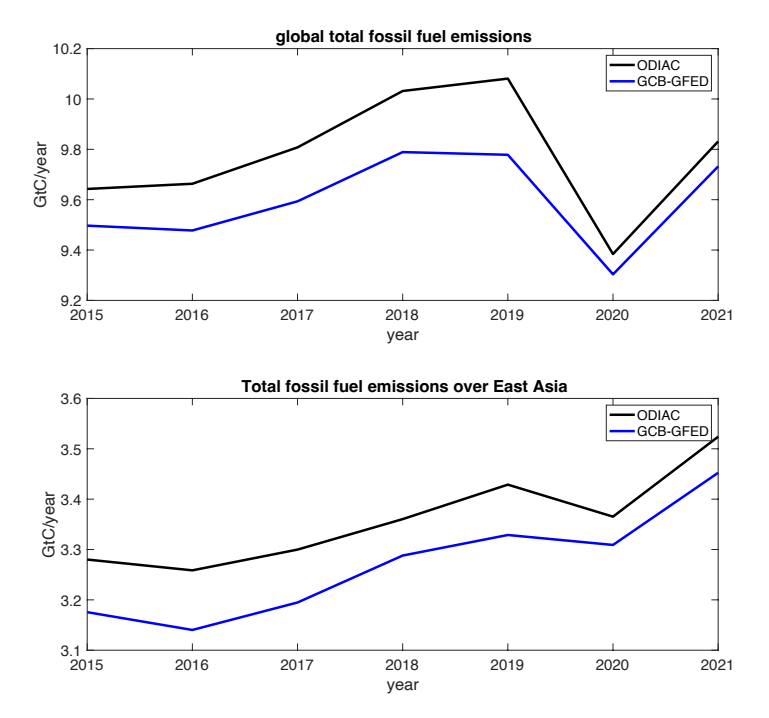


Figure S15 The ODIAC fossil fuel emissions used in this study and the GFED fossil fuel emissions from global carbon budget 2022 (GCB-GFED) have the similar changes during 2015-2021, though the mean difference is about 0.1 GtC/year. Top panel: global fossil fuel emission estimates from ODIAC (black) and GCB-GFED (blue); bottom panel: total fossil fuel emissions over East Asia. Unit: GtC/year.

Science Advances Page 39 of 47

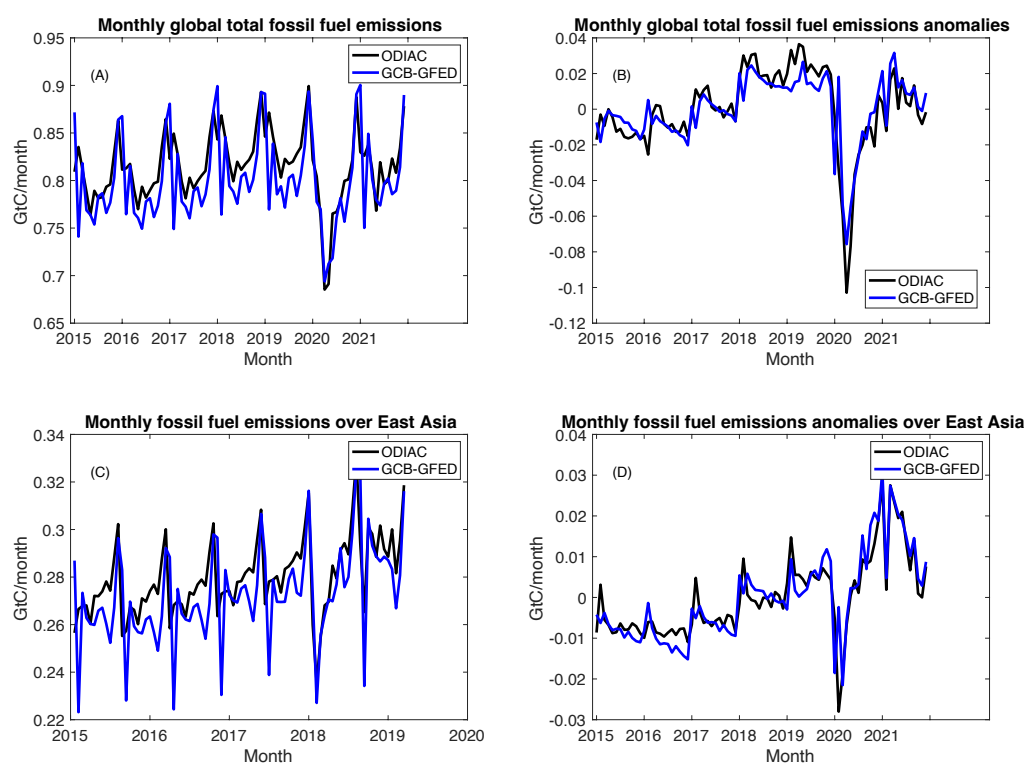
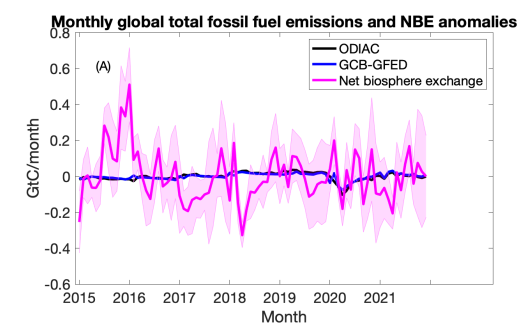


Figure S16 The ODIAC fossil fuel emissions used in this study and the GFED fossil fuel emissions from global carbon budget 2022 (GCB-GFED) have the similar monthly anomalies in both global scale and over East Asia, though these two fossil fuel emissions have different seasonal cycle. (A) Monthly global fossil fuel emission estimates from ODIAC (black) and GCB-GFED (blue) and (B) their anomalies. (C) Monthly fossil fuel emissions over East Asia and (D) their anomalies. Unit: GtC/month.

Science Advances Page 40 of 47



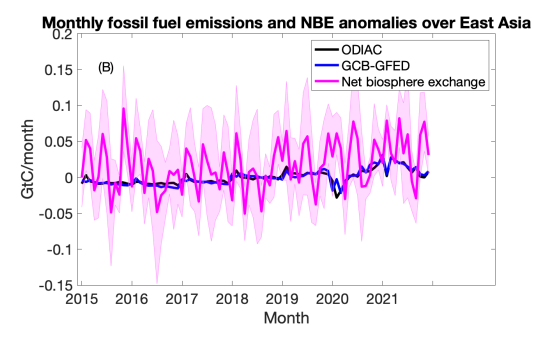


Figure S17 The contrast between monthly NBE anomalies and monthly fossil fuel emission anomalies. (A) Monthly fossil fuel emission anomalies from ODIAC (black) and GCB-GFED (blue), and NBE anomalies (magenta) over the globe and (B) over East Asia. Unit: GtC/month.

Science Advances Page 41 of 47

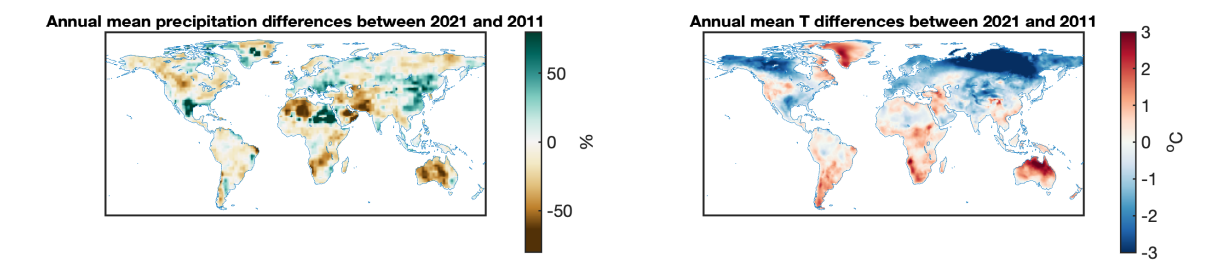


Figure S18 Left panel: annual mean relative precipitation differences between 2021 and 2011 (unit: %). The precipitation differences are normalized by the annual mean precipitation between 2015-2021. Right panel: annual mean temperature differences between 2021 and 2011 (unit: °C).

Science Advances Page 42 of 47

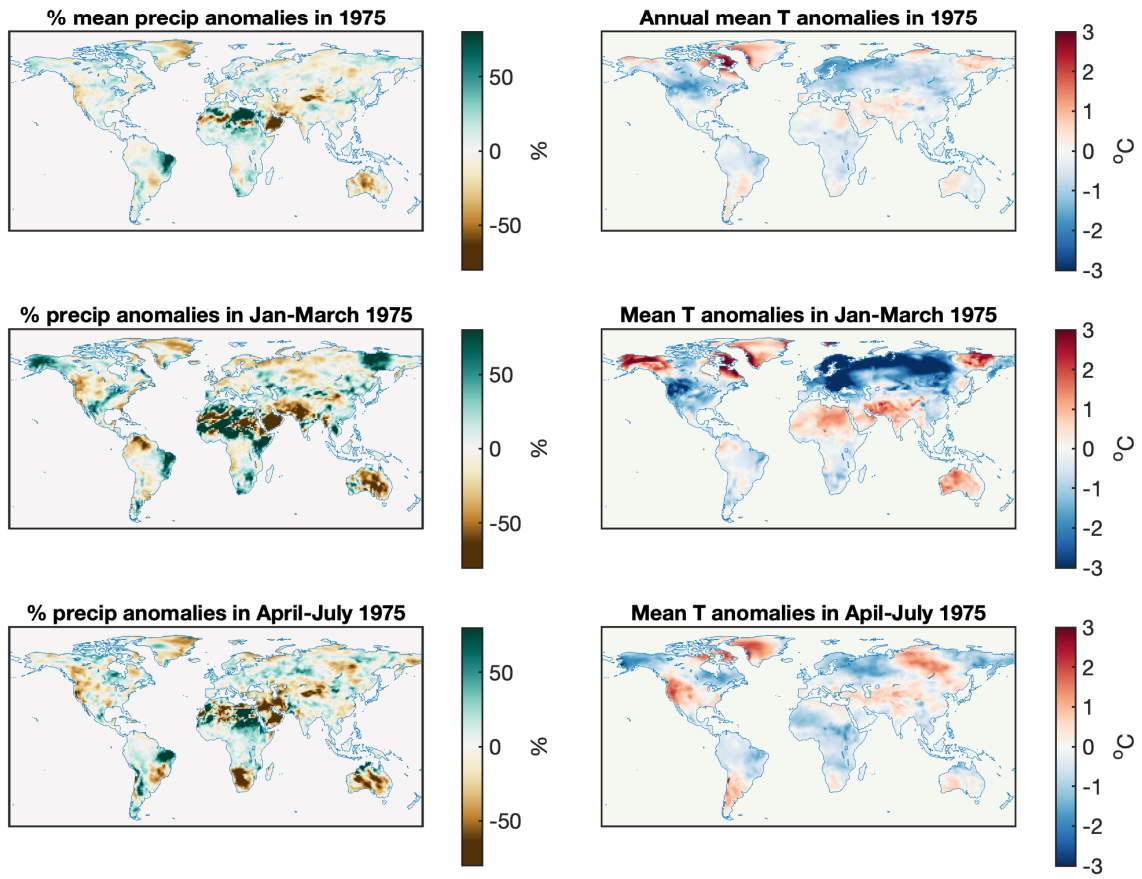


Figure S19 Precipitation and temperature anomalies in 1975. The anomalies were calculated with respect to the mean between 1972 and 1978. Top panels: annual precipitation and temperature anomalies (unit: °C); Middle panel: precipitation and temperature anomalies between Jan-March 1975; Bottom panel: precipitation and temperature anomalies between April-July 1975.

Science Advances Page 43 of 47

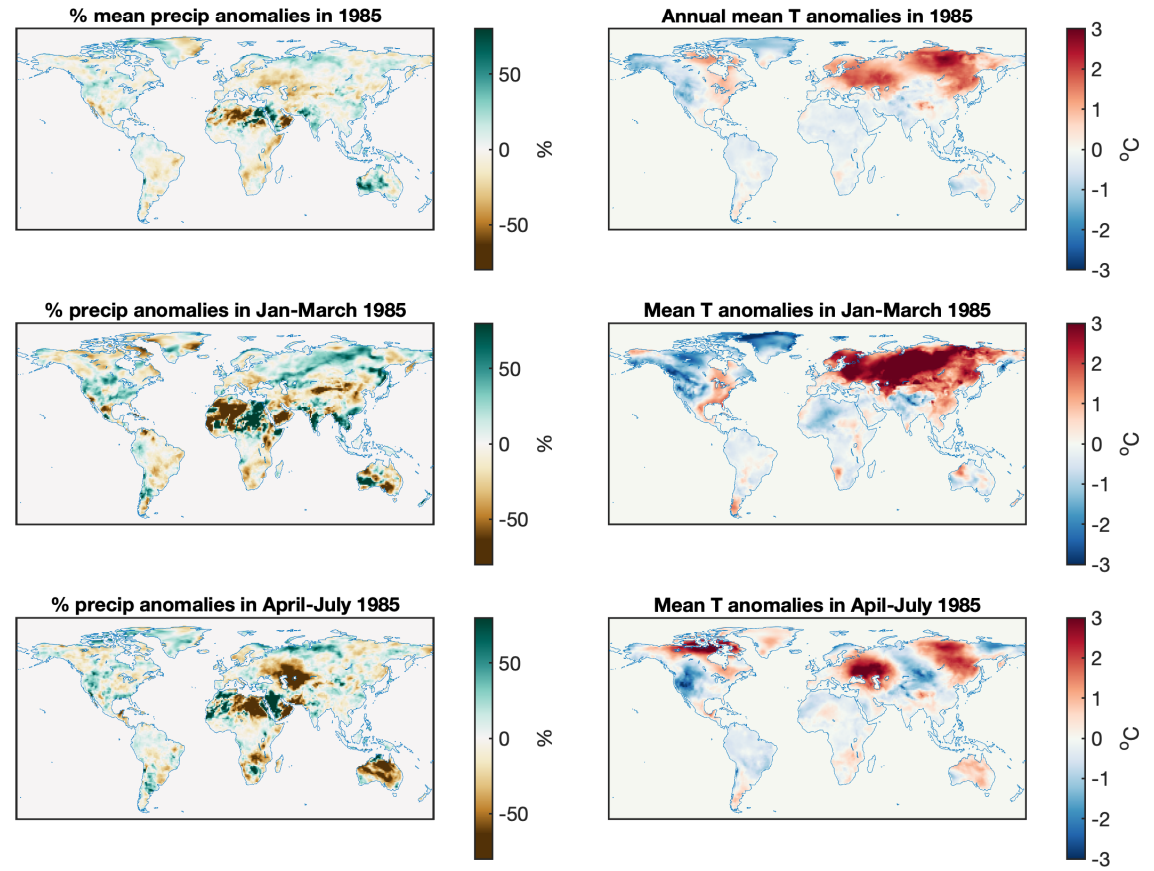


Figure S20 Precipitation and temperature anomalies in 1985. The anomalies were calculated with respect to the mean between 1982 and 1988. Top panels: annual precipitation and temperature anomalies (unit: °C); Middle panel: precipitation and temperature anomalies between January and March 1985; Bottom panel: precipitation and temperature anomalies between April and July 1985.

Science Advances Page 44 of 47

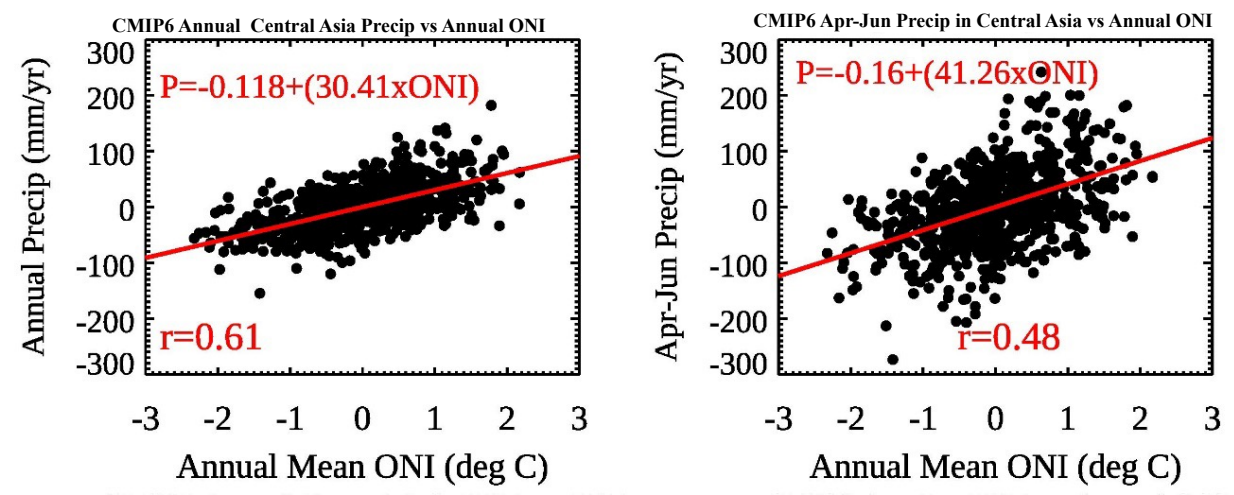


Figure S21 (left) Annual precipitation anomalies over the Central Asian Region (30°E-85°E, 30°N-50°N) versus annual mean Oceanic Niño Index (ONI) for the nine available CMIP6 models which have r1i1p1 versions (described further in the text). (Right) Same as the left panel, except April through June precipitation anomalies. Each dot in each plot represents a seasonal or annual precipitation anomaly for each of the individual model years from 2016-2100. To compute the ONI, any possible long-term trend is linearly removed for each model first; analogously this is how precipitation anomalies are computed. The linear correlation coefficients and best-fit lines are shown in each panel. The Coupled Model Intercomparison Project Phase Six (CMIP6) models used for this analysis are only those which contain r1i1p1 versions, in which "r" refers to the realization (ensemble member), "i" initialization method, and "p" the physics. We utilize nine CMIP6 models (IPSL, CNRM, MPI, NCAR, MRI, CCCMA, MIROC, GFDL, and CAM5). For an overview of the configuration and experimental design of CMIP6, please see (53).

Science Advances Page 45 of 47

Table S1. Summary of the ensemble of top-down atmospheric inversion models.

Model Name	Transpo rt Model	Resolutio n	Inversion Method	Meteorol ogy	Prior terrestrial biosphere flux	Prior air-sea flux	Contact
NOAA- Baker	PCTM	4° x 5°	4D-Var	MERRA2	CASA-GFED3	Landschutzer v4.4	D. Baker
CAMS	LMDZ	1.9°x3.75°	4D-Var	ERA-5	ORCHIDEE	CMEMS	F. Chevallier
John Hopkins	GEOS- Chem	4° x 5°	Geostastica 1/4D-Var	MERRA- 2	CASA- GFED4.1s	Takahashi	S. Miller
TM5- 4Dvar	TM5	2°x3°	4D-Var	ERA-5	SiB-CASA	CT2019	S. Basu
AMES	GEOS- Chem	4° x 5°	4D-Var	MERRA- 2	CASA- GFED4.1s	CT2019	S. Philip/M. Johnson
COLA	GEOS- Chem	4°x5°	EnKF	MERRA- 2	VEGAS	Rodenbeck202	N. Zeng/Z. Liu
CMS-Flux	GEOS- Chem	4°x5°	4D-Var	Merra-2	CADAMOM	MOM6	J. Liu
GCASv2	MOZAR T-4	2.8°x2.8°	EnKF	ERA-5	BEPS	CT2017	F. Jiang

Science Advances Page 46 of 47

Table S2. List of datasets used in the study.

Table 52. List of datasets used in the study.								
ftp.cira.colostate.edu:/ftp/BAKER/OCO2_b10c_10sec_GOOD_r7.nc4								
https://gml.noaa.gov/ccgg/trends/gl_gr.html								
https://zenodo.org/record/8325420								
https://globalecology.unh.edu/data/GOSIF.html								
https://daac.ornl.gov/VEGETATION/guides/FluxSat_GPP_FPAR.html#datadescraccess								
https://origin.cpc.ncep.noaa.gov/products/analysis_monitoring/ensostuff/ONI_v5.php								
https://www.ncei.noaa.gov/data/global-precipitation-climatology-project-gpcp-								
monthly/access/								
https://doi.org/10.6084/m9.figshare.21770624.v1								
ERA-5 reanalysis https://cds.climate.copernicus.eu/cdsapp#!/dataset/reanalysis-era5-								
land-monthly-means?tab=overview								
https://gml.noaa.gov/ccgg/OCO2_v10mip/download.php								
https://daac.ornl.gov/cgi-bin/dsviewer.pl?ds_id=1593								
https://www.nies.go.jp/doi/10.17595/20180208.001-e.html								

Science Advances Page 47 of 47